





# The Complex Structure of the Bulge of M31

Denis Leahy , Traian Craiciu, and Joseph Postma 

Dept. Physics and Astronomy, University of Calgary, Calgary, AB T2N 1N4, Canada

Received 2022 September 21; revised 2022 December 15; accepted 2022 December 22; published 2023 February 16

## Abstract

The bulge of M31 is of interest regarding the nature of galactic bulges and how their structure relates to bulge formation mechanisms and their subsequent evolution. With the UVIT instrument on AstroSat, we have observed the bulge of M31 in five far-ultraviolet (FUV) and near-ultraviolet (NUV) filters at  $1''$  spatial resolution. Models for the luminosity distribution of the bulge are constructed using the UVIT data and the galaxy image fitting algorithm GALFIT. We fit the bulge without the nuclear region with a Sérsic function for the five images and find Sérsic indices ( $\simeq 2.1$ – $2.5$ ) similar to previous studies but smaller  $R_e$  values ( $\simeq 0.5$ – $0.6$  kpc). When fitting the images including the nuclear region, a multicomponent model is used. We use an eight-component model for the FUV 148 nm image, which has the highest sensitivity. The other images (169–279 nm) are fit with four-component models. The dust lanes in the bulge region are recovered in the residual images, which have subtraction of the bright bulge light using the multicomponent models. The dust lanes show that M31’s nuclear spiral is visible in absorption at NUV and FUV wavelengths. The bulge images show boxy contours in all five UVIT wave bands, which is confirmed by fitting using GALFIT. The Sérsic indices of  $\sim 2.1$ – $2.5$  are intermediate between the expected values for a classical bulge and for a pseudobulge. The boxiness of the bulge provides further evidence that M31’s bulge has contributions from a classical bulge and a pseudobulge.

*Unified Astronomy Thesaurus concepts:* [Andromeda Galaxy \(39\)](#); [Galaxy bulges \(578\)](#); [Galaxy structure \(622\)](#); [Ultraviolet astronomy \(1736\)](#)

## 1. Introduction

Galaxies in the local universe have clear morphological structures, including bulges, disks, and galactic halos.<sup>1</sup> In the widely accepted  $\Lambda$ CDM cosmology, galaxies, as well as their structures, are formed through initial density perturbations in dark matter halos followed by hierarchical buildup (accretion) of gas and various fragments of different sizes. In the early universe, galactic evolution was governed by rapid and violent mergers, dissipative collapse, and hierarchical clustering. As the universe expanded and merger events became less common, rapid evolutionary processes gave way to slow and persistent processes. For galactic bulges, the review of Kormendy & Kennicutt (2004, hereafter [KK04](#)) summarizes bulge structure, morphology, and formation/evolutionary processes. [KK04](#) posit that in the late universe galactic evolution manifests primarily through internal secular processes. This occurs through the slow and steady interaction between various internal galactic components such as the nucleus, bulge, bar, and spiral arms.


Simulations are used to study the formation of disks and spheroids (bulges and halos) in the currently accepted  $\Lambda$ CDM cosmology (e.g., the simulations of Scannapieco et al. 2011 for Milky Way–mass halos). From such simulations the general picture is that bulges form early in the history of a galaxy and that disks are relatively young (e.g., Brooks & Christensen 2016; Tonini et al. 2016). Other studies focus on observational

characteristics of galaxies and their structure. For example, Wuyts et al. (2011) examine the dependence of galaxy structure on galaxy position in the star formation rate (SFR) versus mass diagram.<sup>2</sup> Other relevant results from Wuyts et al. (2011) are as follows: the Sérsic index is  $n \sim 1$ – $1.5$  for star-forming main-sequence galaxies and  $n \gtrsim 3$  for red clump galaxies. The observational study by Querejeta et al. (2021) examines galactic structures and their relation to molecular gas and star formation in nearby galaxies.

Two categories of galactic bulges emerge from the dichotomy between galactic evolution in the early and late universe ([KK04](#)). The “classical” bulge is interpreted within the framework of the Hubble–Sandage–de Vaucouleurs classification scheme to represent an “elliptical living in the middle of a disk,” probably formed through a merger event. In contrast, if a bulge’s evolution is dominated by internal secular processes, it becomes a “pseudobulge.” While [KK04](#) recognized difficulties in classifying intermediate cases, the basic interpretation is this: if a bulge has elliptical shape, it is a classical bulge, while a bulge with disk-like properties is a pseudobulge. In this manner, M31’s bulge has been classified as a classical bulge, along with other galaxies such as M81 and the Sombrero galaxy (NGC 4594), which show bulges that are rounder than their associated disks.

Evidence in support of the classical bulge formation theory has existed since the early simulations of Toomre (1977). Evolutionary formation simulations by Naab & Burkert (2003) and Bournaud et al. (2005) suggest that mergers of same-size disk galaxies have as a likely outcome a larger elliptical galaxy, while a greater mass ratio for the colliding disk galaxies results

<sup>1</sup> Galactic halos refer to the extended outer parts of galaxies, which are distinct from the dark matter halos that are well studied in cosmological simulations and that provide the gravity wells for early galaxy formation.

 Original content from this work may be used under the terms of the [Creative Commons Attribution 4.0 licence](#). Any further distribution of this work must maintain attribution to the author(s) and the title of the work, journal citation and DOI.

<sup>2</sup> This diagram separates galaxies into two main categories: star-forming galaxies, referred to as the star-forming main sequence, and passive (non-star-forming) galaxies, referred to as the red clump. Observations show that the difference in structure between the two types of galaxies is already in place by redshift  $\sim 2.5$ .

in a spiral galaxy with a large elliptical bulge and with Sérsic index  $n < 2$ . This supports the theory of the bulge being an elliptical galaxy residing within a larger spiral structure. A number of major merger simulations have found that the bulge of the resulting galaxy is a pseudobulge, with significant rotation, e.g., for the merger of two gas-rich pure disk galaxies (Keselman & Nusser 2012). The major merger study by Athanassoula et al. (2016) finds that most stars in the disks of merging galaxies form a classical bulge, with the remaining stars and stars born during the merger forming a thick disk and bar. After the merging phase, a disky pseudobulge and a thin disk grow. The thin disk has the youngest stars, the pseudobulge has a wide range of ages, and the classical bulge has the oldest stars.

It has been proposed that bulges can also take shape from instabilities in the early disk, with large clumps and star clusters collapsing inward toward the center owing to dynamical friction. Noguchi (1999) describes galactic bulge formation by the inward transport of disk matter in the early history of a galaxy. In a chemodynamical simulation of galaxy formation, Immeli et al. (2004) found that when the cold gas in the nascent galaxy cools efficiently, massive clumps form that spiral inward to form a central bulge. In contrast, slow cooling of the initial cold clouds leads to star formation in a more quiescent manner, with instabilities setting in later and resulting in a smaller bulge with a prominent stellar bar. The idea that clumps in the galaxy interact with the disk to provide fuel for both spiral and bulge structure is supported by the study of Bournaud et al. (2005).

The problem with bulge classification stems from the fact that internal secular evolution leads to an accumulation of dense components in the centers of disk galaxies that look similar to bulges built from classical mergers. The pseudobulges of the former were made slowly from disk gas, or largely influenced by the dynamics of the internal galactic components (Mould 2013). KK04 prescribe several key factors that can be used to identify a pseudobulge: it has a flattened shape, similar to its corresponding disk; it contains a nuclear bar (in relatively face-on galaxies); it is box-shaped (in relatively edge-on galaxies); it has a Sérsic index between 1 and 2; and it is more rotation dominated than classical bulges. It is apparent that a simple morphological assessment will not suffice and one must implement a quantitative fit to surface photometry to differentiate between classical and pseudobulges (Mould 2013).

For the detailed study of galactic structure, dynamics, and evolution, there is no better astrophysical laboratory than our closest neighboring spiral galaxy, the Andromeda galaxy (M31), at a distance of  $785 \pm 25$  kpc (McConnachie et al. 2005). Our external view of M31 and its high Galactic latitude (and thus low Galactic extinction) allow studies of the M31 bulge with a clearer view than comparative studies of our own Galactic bulge.

There are several lines of evidence suggesting that internal secular evolutionary processes have taken place throughout M31's history and have had a significant impact on its structure and dynamics. Gordon et al. (2006) find an offset star-forming ring in the bulge region outside of the nuclear spiral that is interpreted as a strong indicator of internal interactions between the structural components of M31. A mid-infrared survey of the morphology and surface brightness profiles of M31's components by Barmby et al. (2006) shows the complex interactions

between the nuclear region, bulge, and disk. In HI mapping by Chemin et al. (2009), several ring-like and spiral-like structures are observed, with additional HI structures discovered in the outskirts of the disk, all thought to be the result of complex internal interactions.

On the other hand, a history of external hierarchical formation for M31 is supported by several studies. Evidence for past interactions between M31 and its nearby dwarf companions M32 and NGC 205 was given by Ibata et al. (2001). The presence of many substructures in the halo is taken as evidence of numerous ( $\sim 16$ ) accretion events involving dwarf galaxies (Tanaka et al. 2010). A study of the rotational kinematics and metallicities of the M31 globular cluster system (Bekki 2010) concluded that an ancient major merger event is highly probable. Veljanoski et al. (2014) analyze the kinematics of the outer halo globular cluster system of M31, concluding that a significant fraction of the globular clusters in the outer halo were accreted with their parent dwarf galaxies. Simulations by Hammer et al. (2018) conclude that a major merger  $\sim 2$ – $3$  Gyr ago explains the long-lived 10 kpc star-forming ring in M31, the absence of a remnant for the giant stream, and the spatial distribution of other major structures in M31's halo. D'Souza & Bell (2018) argue that many of M31's unusual features (disk heating, tidal structures, massive and metal-rich halo) can be explained by a dominant merger  $\sim 2$  Gyr ago, with M32 the remnant core of the merger progenitor. McConnachie et al. (2018) analyze the structure of M31's halo to find that the 13 most distinctive substructures were produced by at least five different accretion events, all in the past 3 or 4 Gyr, and that a few of the large structures may have been produced by a single event.

Thus, there is plentiful evidence for the significance of mergers and of secular evolution over M31's history. Analyses of structural parameters for M31's bulge, relevant to the classical versus pseudobulge question, have been carried out using observations in infrared and optical. Seigar et al. (2008) present an updated mass model for M31 and find that adiabatic collapse of the halo is favored for M31, which favors secular (rather than merger-driven) bulge formation, as the gradual accumulation of central mass increases the likelihood that adiabatic collapse will operate. The analysis of Saglia et al. (2010) finds that the bulge is mainly old and of solar metallicity ( $\gtrsim 12$  Gyr), with a younger component in the inner few arcseconds with metallicity  $\sim 3$  times solar. The existence of mixed stellar populations in the bulge is confirmed by subsequent studies (e.g., Dong et al. 2018; Leahy et al. 2022b). Courteau et al. (2011) obtain structural parameters for its Sérsic bulge (Sérsic index ( $n \simeq 2$ ), effective radius  $R_e \simeq 1$  kpc), exponential disk, and power-law-with-core halo. Based on the ratio of bulge to disk scale lengths and on the Sérsic index, they conclude that M31 likely evolved through early "classical" merging with structural readjustments caused by secular evolution and satellite accretion. Dorman et al. (2013) find  $n \simeq 2$ , a smaller bulge ( $R_e = 0.77 \pm 0.03$  kpc), and varying luminosity functions with radius. Opitsch et al. (2018) show that kinematics data support a bar in M31, with nontriaxial streaming motions. The presence of a bar is confirmed by Feng et al. (2022) in the central  $4.6$  kpc  $\times$   $2.3$  kpc region of M31. Saglia et al. (2018) find that the bar and bulge are similar in age and  $[\alpha/\text{Fe}]$  maps, but the bar stands out in metallicity, approximately solar, in contrast to the metal-rich bulge. Blańa Díaz et al. (2018) construct models for the M31 bulge,

including classical bulge and box/peanut bulge, and find that both components are required to fit the data.

In this study we analyze the structure of M31’s bulge at ultraviolet wavelengths. The data are from the M31 UVIT survey (Leahy et al. 2020), which was carried out in far-ultraviolet (FUV) and near-ultraviolet (NUV) by the UVIT instrument (Tandon et al. 2017) on AstroSat (Singh et al. 2014). Some previous results on UVIT FUV and NUV studies of the M31 bulge include detection of young hot stars in the bulge (Leahy et al. 2018), analysis of the radial surface brightness distribution of the bulge (Leahy et al. 2021b), detection and characterization of FUV variable sources in the bulge (Leahy et al. 2021a) by comparison of two epochs of observation, analysis of the FUV to far-infrared spectral energy distribution (SED) of the M31 bulge to study the star formation history of M31 (Leahy et al. 2022b), and an SED analysis of the UVIT and PHAT photometry of clusters in the northern disk of M31 (Leahy et al. 2022a).

The structure of the bulge of M31 is analyzed in detail here using the two-dimensional surface brightness modeling software GALFIT (Peng et al. 2002). In Section 2.1 we briefly describe the FUV and NUV images of the bulge of M31. Section 2.2 describes GALFIT briefly and the process of modeling the surface brightness distribution of the M31 bulge. Section 3.1 describes the process and the results of modeling the outer bulge omitting the nuclear region’s light distribution, and Section 3.2 presents the resulting models incorporating the nuclear region. Position offsets between the centers of the components and of the nucleus and bulge asymmetry are discussed in Section 3.3. GALFIT’s performance is reviewed in Section 4.1. Comparison with previous measurements of the structure of M31’s bulge at other wavelengths is given in Section 4.2, and the phenomenological nature of our multi-component fits is discussed in Section 4.3. The classical versus pseudobulge nature of M31’s bulge is discussed in Section 4.4, including Sérsic index and boxiness indicators. We reveal the nuclear spiral in FUV and NUV wave bands using the model-subtracted residual images in Section 4.5, and we conclude with a summary in Section 5.

## 2. Observations and Bulge Modeling

### 2.1. Observations

The AstroSat observatory and its science capabilities are described by Singh et al. (2014). The UVIT instrument, its filters and its calibration are described by Tandon et al. (2017). UVIT has 1'' spatial resolution and a circular field of view with diameter  $\sim 28'$ . Observations were obtained in FUV, with F148W and F172M filters, and in NUV, with N219M and N279N filters, as part of the M31 UVIT survey (Leahy et al. 2020). The survey covered the sky area of M31 with 19 different fields, with planned exposures in FUV and NUV filters for each field. The filters used were F148W, F169M, F172M, N219M, and N279N, with one field observed in F154W. With the failure of the NUV detector partway through the survey, only about half of the fields were observed in NUV (see Table 1 of Leahy et al. 2020). The field 8 observation was missed in the initial survey. The nominal exposure for each observation was 10,000 s, but in practice the exposure times varied from  $\simeq 2000$  to 10,000 s.

The astrometry was calibrated using star positions from Gaia using the CCDLAB UVIT processing software (Postma

**Table 1**  
UVIT Observations for Field 1

UVIT Filter	Observation (BJD) <sup>a</sup>	Exposure Time (s)	Counts	Mean S/N per arcmin <sup>2</sup>
F148W	A: 2,457,671	7736	$1.04 \times 10^7$	
F148W	B: 2,458,805	17,191	$2.39 \times 10^7$	
F148W	C: 2,459,183	12,632	$1.75 \times 10^7$	
F148W	A+B+C <sup>b</sup>	38,299	$5.27 \times 10^7$	288
F169M	2,458,804	10,427	$9.50 \times 10^6$	122
F172M	A: 2,457,672	3612	$1.63 \times 10^6$	
F172M	B: 2,458,805	18,057	$8.74 \times 10^6$	
F172M	A+B <sup>b</sup>	21,789	$1.05 \times 10^7$	128
N219M	2,457,671	7781	$6.05 \times 10^6$	97.4
N279N	2,457,672	3627	$5.70 \times 10^6$	94.6

**Notes.**

<sup>a</sup> Barycentric Julian date.

<sup>b</sup> Combined images for F148W and F172M were used in the analysis here.

& Leahy 2017). Because of the differing exposures and sensitivities in each filter, the limiting AB magnitudes varied slightly between fields. The limiting AB magnitudes are given by the histograms in the top panel of Figure 6 in Leahy et al. (2020): F148W—23.2; F154W—23.4; F169M—23.4; F172M—22.2; N219M—22.4; N279N—21.4. The detector is a photon counting detector: a photocathode followed by a microchannel plate amplifier, then a phosphor to convert the electron cloud into a light shower that is detected by a CMOS array. Cosmic-ray tracks are removed using the CCDLAB software, resulting in a very low background where noise is dominated by Poisson statistics. For example, the F148W image with observation in 2016 October had  $1.04 \times 10^7$  photon counts, over a circular field covering  $1.32 \times 10^7$  pixels. This gives a mean number of counts and signal-to-noise ratio (S/N) over a 1' square region of  $1.63 \times 10^4$  and 128, respectively.

Additional UVIT observations of the bulge (Field 1) in F148W, F169M, and F172M filters took place  $\sim 3.1$  yr later. Table 1 of Leahy et al. (2021a) lists both sets of observations of the bulge field (Field 1). A third observation of Field 1 was obtained a year later. Table 1 gives the filters, observation dates, exposure times, and mean S/N for a 1' square region of each image used in this analysis. All images were produced using CCDLAB (Postma & Leahy 2017), including combining the three F148W observations and two F172M observations to produce single deeper exposures in those filters.

### 2.2. M31 Bulge Modeling Using GALFIT

Two-dimensional modeling of the M31 bulge and nucleus light distribution in NUV and FUV was carried out using the galaxy image fitting program GALFIT developed by Peng et al. (2002). GALFIT is capable of modeling well-resolved galaxy images with multiple components, which enables extraction of galactic substructures that are otherwise hidden. GALFIT was designed to model bulges, disks (including spiral arm structure), and halos of galaxies by fitting their images. Various functional forms for the different components, as well as linear combinations of those functions, can be used. The functions are elliptical (functions of an elliptical radial coordinate), with four parameters: two for the center ( $x_c, y_c$ ), and two for the ellipse (ellipticity  $q$  and major-axis position angle  $\theta_{PA}$ ). Generally a uniform background level of the image is included (one parameter).

GALFIT carries out a model fit by the creation of model images, convolution with the point-spread function (PSF), and subsequent comparison of the model with the data. The noise image can be calculated by GALFIT for the case that the image data are photon counts (Poisson statistics), which is the case for the UVIT images. The best-fit model parameters are found by minimizing  $\chi^2$  using the Levenberg–Marquardt downhill gradient method. The output of GALFIT includes the best-fit parameters, the model image, and the residuals between the model and the data.

### 2.2.1. Summary of GALFIT Radial Profiles

The Sérsic function is defined as

$$\Sigma(r) = \Sigma_e \exp \left[ -\kappa \left( \left( \frac{r}{r_e} \right)^{1/n} - 1 \right) \right]. \quad (1)$$

The Sérsic function has seven parameters, including the elliptical parameters:  $x_c$ ,  $y_c$ ,  $m_{\text{tot}}$ ,  $r_e$ ,  $n$ ,  $q$ ,  $\theta_{\text{PA}}$ , with  $m_{\text{tot}}$  the integrated magnitude,  $r_e$  the effective radius, and  $n$  the Sérsic index. The exponential profile has the form

$$\Sigma(r) = \Sigma_0 \exp \left( \frac{-r}{r_s} \right), \quad (2)$$

with six parameters:  $x_c$ ,  $y_c$ ,  $m_{\text{tot}}$ ,  $r_s$ ,  $q$ ,  $\theta_{\text{PA}}$ . The Gaussian profile has the form

$$\Sigma(r) = \Sigma_0 \exp \left( \frac{-r^2}{2\sigma^2} \right), \quad (3)$$

with six parameters:  $x_c$ ,  $y_c$ ,  $m_{\text{tot}}$ , FWHM,  $q$ ,  $\theta_{\text{PA}}$ , with FWHM =  $2.354\sigma$ . The Moffat profile is given by

$$\Sigma(r) = \frac{\Sigma_0}{[1 + (r/r_d)^2]^n}, \quad (4)$$

with  $r_d = \frac{\text{FWHM}}{2\sqrt{2^{1/n} - 1}}$ . The seven parameters are  $x_c$ ,  $y_c$ ,  $m_{\text{tot}}$ , FWHM, concentration index  $n$ ,  $q$ , and  $\theta_{\text{PA}}$ . The Nuker profile takes the form

$$I(r) = I_b 2^{\frac{\beta-\gamma}{\alpha}} \left( \frac{r}{r_b} \right)^{-\gamma} \left[ 1 + \left( \frac{r}{r_b} \right)^\alpha \right]^{\frac{\gamma-\beta}{\alpha}}. \quad (5)$$

The Nuker profile has a total of nine free parameters:  $x_c$ ,  $y_c$ ,  $\mu_b$ ,  $r_b$ ,  $\alpha$ ,  $\beta$ ,  $\gamma$ ,  $q$ ,  $\theta_{\text{PA}}$ , with  $\mu_b$  the surface brightness at radius  $r_b$ . Additional available functions are described in Peng et al. (2002) and the GALFIT documentation on the GALFIT web page.<sup>3</sup>

### 2.2.2. UVIT Point-spread Function

To account for telescope optics and, for ground-based telescopes, atmospheric seeing, GALFIT convolves the model image with a PSF image. To extract the PSF image for each UVIT filter, the following process was implemented. For the UVIT image in each filter, several isolated point-source stars were identified. From these we chose one where the star was best centered in the  $5 \times 5$  array of pixels around the star. CCDLAB produces images with  $0''.4168$  pixels, which was

designed to oversample the instrument resolution of  $\simeq 1''$  by a factor of  $\sim 2.5$ . Because the PSF has extended wings (Tandon et al. 2017), we selected a subimage of  $55 \times 55$  pixels centered on the point source. Because there is diffuse light in M31, e.g., from the bulge and disk, we subtracted the mean of the four  $7 \times 7$  pixel corners from the image to produce the diffuse background-subtracted PSF. The GALFIT modeling for each UVIT filter image of M31 utilized the corresponding filter's PSF fits image.

### 2.2.3. Modeling the M31 Bulge Structure in the Five UVIT Filters

To model as much of the bulge light as possible while avoiding the light from the disk and inner spiral arms, the central  $1001 \times 1001$  pixel ( $417''.2 \times 417''.2$ ) area of Field 1 was chosen. We visually inspected larger regions (1101 and 1201 pixels) but could see some light from the spiral arms in those images at the corners, so we rejected use of larger regions. The image of the chosen region is shown in Figure 1 for the five UVIT FUV and NUV filters: F148W, F169M, F172M, N219M, and N279N.

An initial array of GALFIT tests was performed with the goal of determining the approximate fit qualities of the different radial profile functions of GALFIT (we tested the five functions listed in Section 2.2.1) for both the bulge and nucleus using the F148W image. The model included the three brightest stars in the chosen  $1001 \times 1001$  pixel area.<sup>4</sup> The Sérsic, Gaussian, Moffat, Nuker, and PSF functions in GALFIT were used as model components in trials where up to two components were used to fit the bulge region. All model components were elliptical (Peng et al. 2002) because galactic components (e.g., bulge, disk, and halo) projected onto a two-dimensional image are elliptical in shape.

Next, we carried out model fits to test the constancy of the model parameters versus wavelength. Three separate series of tests with a Sérsic bulge and a Moffat nucleus were performed with (i) all free parameters, (ii) a constant effective radius, and (iii) a constant Sérsic index. After performing an analysis of the parameters versus wavelength for each of the three tests, we conclude that none of the parameters are consistent with being constant versus wavelength. Thus, further modeling requires Sérsic index, FWHM, or concentration index as free parameters for each UVIT filter.

### 2.2.4. Dust Mask

Dust cloud absorption features are visible northwest of the center of the bulge in the UVIT images (see the panels for the various filters in Figures 1(a)–(e)). We excluded the areas with strong dust cloud features from the fits by using a mask because our purpose was to fit the bulge structure and not the dust clouds. We used a Python script to generate a list of pixels that correspond to the coordinates of the pixels affected by the main dust cloud regions visible in the bulge. The F148W image was used to identify the dust clouds owing to its better S/N compared to the images taken with the other four filters. The mask is shown in Figure 1(f) and was used for the model fits for all five UVIT filters.

<sup>3</sup> The GALFIT home web page is at <https://users.obs.carnegiescience.edu/peng/work/galfit/galfit.html>.

<sup>4</sup> The fourth-brightest star had significantly less flux.

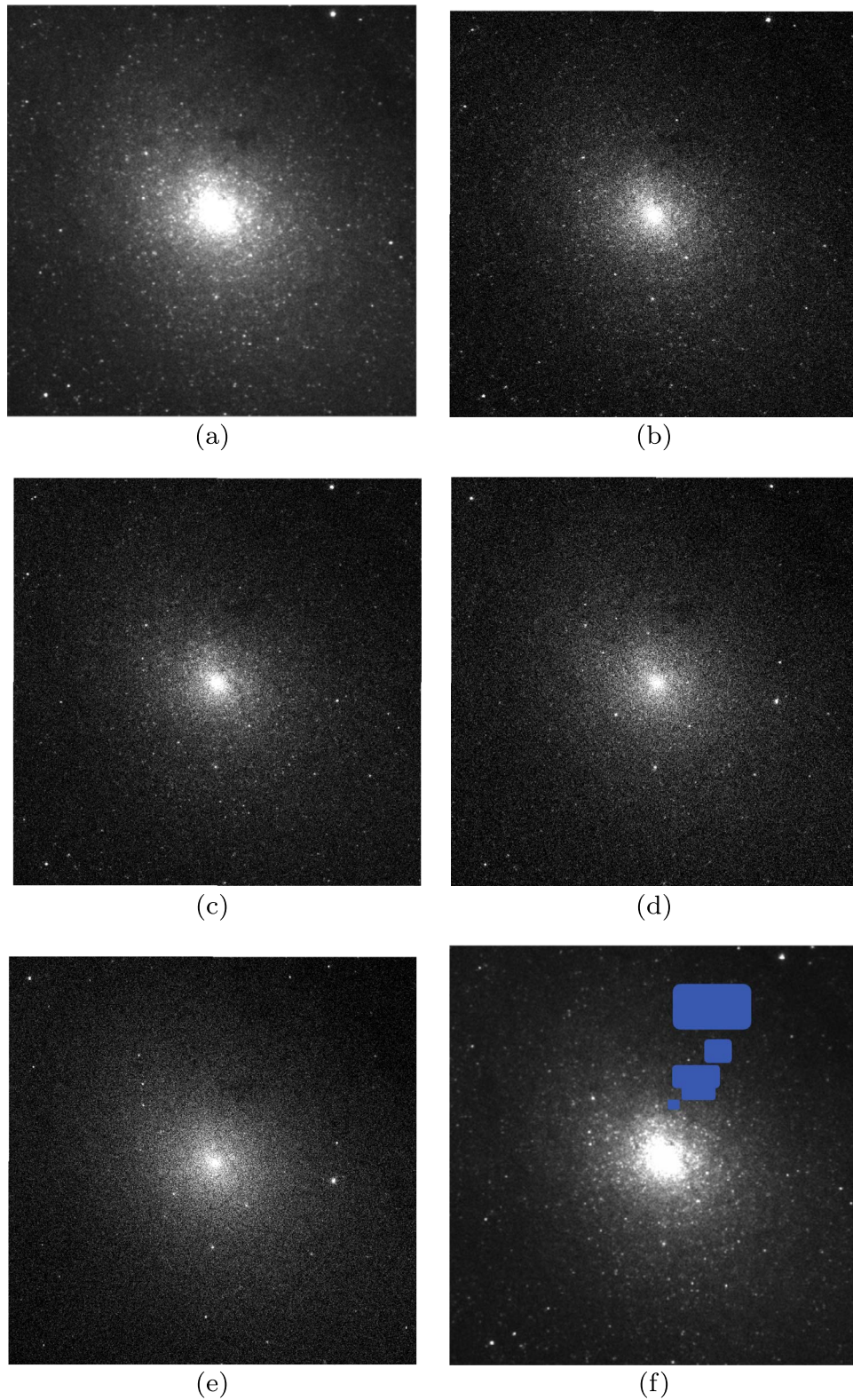


**Figure 1.** UVIT  $1001 \times 1001$  pixel ( $417'' \times 417''$ ) images of the M31 bulge in (a) F148W filter, (b) F169M filter, (c) F172M filter, (d) N219M filter, (e) N279N filter, and (f) F148W filter with dust mask. The dust mask used to omit the dust cloud features is marked in blue in the F148W image. The pixel size is  $0''.4168$ .  $1''$  at M31's distance is 3.81 pc.

### 2.2.5. Bright Stars and Background

In addition to the stellar light from the bulge, there are several bright foreground stars in the image. We test adding a different number of stars in the model for the bulge. Rows 4–6

of Table 2 show the  $\chi^2$  for model fits including the bulge (Sérsic plus Gaussian) plus one, two, or three stars for comparison to the  $\chi^2$  for a bulge model with a Sérsic plus Gaussian and no stars (row 3). Including the brightest star, the two brightest stars, or the three brightest stars successively

**Table 2**

Comparison of Fits for Models with and without Bright Stars for F148W Image

Bulge/ Nucleus	Star 1	Star 2	Star 3	$\chi^2$	No. Free Parameters
Sérsic	...	...	...	728,365	8
Sérsic, PSF	...	...	...	723,354	11
Sérsic, Gauss <sup>a</sup>	...	...	...	719,700	14
Sérsic, Gauss	Gauss	...	...	704,212	20
Sérsic, Gauss	Gauss	Gauss	...	702,767	26
Sérsic, Gauss	Gauss	Gauss	Gauss	698,236	32

**Note.**<sup>a</sup> Gauss stands for a Gaussian function.

improves the  $\chi^2$  by  $\sim 15,000$ ,  $\sim 1500$ , and  $\sim 4500$  compared to no stars.<sup>5</sup>

We did not include more stars because the improvement in fit quality ( $\chi^2$ ) was significantly less than for the three brightest stars. For all of the fits presented here the background and the positions and magnitudes of the three brightest stars are free parameters (three per star), to give the number of background plus star parameters of 10.

### 2.2.6. Nucleus Mask

The nucleus of M31 has a complex structure as shown by Peng (2002), which includes the compact nucleus and the nuclear bulge surrounding it. The compact nucleus was resolved into double components by Lauer et al. (1993) with Hubble Space Telescope (HST) Wide Field and Planetary Camera (WFPC) observations. The HST WPC2 F555W (*V*-band) image was analyzed by Peng (2002) using GALFIT two-dimensional fitting of the central  $5'' \times 5''$  area. Kormendy & Bender (1999) show that the double nuclei in *V* band (called P1 and P2) are the two ends of an eccentric disk of stars orbiting the central black hole, which has mass  $\sim 3 \times 10^7 M_\odot$ . Peng (2002) finds that the central region is well modeled by four physical components: P1, P2, the M31 elliptical ( $q \simeq 0.81$ ) bulge, and a spherical nuclear bulge ( $R_e \simeq 3''.2$ ).

In order to fit the brightness distribution of the bulge only, we exclude from the fit the emission associated with the nucleus (compact nucleus plus nuclear bulge). For this purpose a series of GALFIT pixel masks of square shape and varying size, centered on the nucleus, were created. The best-fit  $\chi^2$  was given by the nucleus pixel mask of dimensions  $41 \times 41$  pixels ( $17'' \times 17''$ ). Table 3 shows the results of tests conducted to verify whether masking the nuclear region improves the fit of the bulge. The  $\chi^2$  is reduced at high significance (several tens of  $\sigma$ ; Press et al. 1992),<sup>6</sup> indicating that there is a separate component (the nucleus) smaller than the  $41 \times 41$  pixel mask. The fact that the bulge region is fit significantly better with the nuclear mask for the tested cases (one-Sérsic, two-Sérsic, and three-Sérsic functions) is a strong indicator that the nuclear region has additional components, in agreement with the results of Peng (2002). Hereafter, when fitting the “bulge only,” the nucleus mask is included to omit the nuclear region (see

<sup>5</sup> The reason that these values are not monotonically decreasing with decreasing brightness of the stars is because the location of the stars relative to the bulge center has a significant effect.

<sup>6</sup> The reduction in  $\chi^2$  is much larger than the reduction in degrees of freedom (1681 for the  $41 \times 41$  pixel mask).

**Table 3**Comparison<sup>a</sup> of Fits for Models with and without Nucleus Mask for F148W Image

Bulge Components	$\chi^2$ with Mask	$\chi^2$ with- out Mask	$\Delta\chi^2$	No. Free Parameters
Sérsic	685,595	698,695	-13,099	8
Two Sérsic	673,491	683,950	-10,459	15
Three Sérsic	670,345	682,471	-12,126	22

**Note.**<sup>a</sup> Model fits include the dust mask.**Table 4**Comparison<sup>a</sup> of Fits for Models with and without Fixed Primary Sérsic Index ( $n = 2$ ) for F148W Image

Bulge Components	$\chi^2$ ( $n = 2$ )	$\chi^2$ ( $n$ Free)	$\Delta\chi^2$	No. Free Parameters <sup>b</sup>
Sérsic	686,199	685,595	-604	7, 8
Two Sérsic	673,491	673,491	-447	14, 15
Three Sérsic	670,736	670,345	-391	21, 22

**Notes.**<sup>a</sup> Model fits include the dust mask and nucleus mask.<sup>b</sup> The fits with  $n$  fixed have one fewer parameters.

Section 3.1). When fitting the bulge plus nucleus, the nucleus mask is omitted, to include the nuclear region (see Section 3.2).

## 3. Results

### 3.1. Model for the Bulge without Nuclear Region

As determined by the tests above, we include the dust mask, the nucleus mask, and the three brightest stars to find a model for the bulge only, omitting the complex nuclear region (Peng 2002). The bulge model was gradually increased in complexity by starting with a single Sérsic function and then adding additional Sérsic functions to improve the model fit.<sup>7</sup>

A Sérsic index  $n \sim 2$  has been previously suggested for M31 (e.g., Courteau et al. 2011). Thus, we compare the models in Table 4 with the primary Sérsic function (defined as the one with the brightest magnitude) fixed at  $n = 2$  to models with a free index. Comparing similar complexity fits (row 1 with row 4, row 2 with row 5, row 3 with row 6), we see that the improvements in  $\chi^2$  by adding one free parameter (the free primary Sérsic index) are 604, 447, and 391, respectively. These values are all highly significant decreases in  $\chi^2$ , showing that the free primary Sérsic index models are better (by  $20\sigma$  to  $25\sigma$  for change in one parameter; Press et al. 1992) than the  $n = 2$  cases. Table 5 lists the parameters for the three-Sérsic models for the bulge (rows 3 and 6 of Table 2). The model with primary Sérsic index fixed at  $n = 2$  has an unrealistically large effective radius:  $2240''$  at the distance of M31 is 8.5 kpc, which can be compared to values of 1.0 kpc from Courteau et al. (2011) and 0.8 kpc from Dorman et al. (2013). This indicates that the  $n = 2$  fit is unrealistic. Hereafter we allow the Sérsic indices of the Sérsic components to be free parameters.

Having determined that Sérsic index should be a free parameter, we present the series of fits to the bulge only (using

<sup>7</sup> Other functions besides Sérsic were tested, including Moffat and Gaussian, but Sérsic functions gave the best results and so are presented here.

**Table 5**  
Comparison of Three Sérsic Bulge Model Parameters with Primary Sérsic (Sérsic1) Index Free and Fixed ( $n = 2$ )

Model	Component	F148W AB Magnitude	Effective Radius		Sérsic Index
			(arcseconds)	(kpc)	
Primary Sérsic index free	Sérsic1	13.30	86.2	0.328	1.48
	Sérsic2	14.67	197	0.750	0.31
	Sérsic3	12.78	393	1.50	1.12
Primary Sérsic index $n = 2$	Sérsic1	9.83	2240	8.53	2.00
	Sérsic2	13.96	70.0	0.266	1.39
	Sérsic3	11.22	1100	4.19	2.65

**Table 6**  
Comparison of Fits for Bulge-only Models<sup>a</sup> and Bulge plus Nuclear Region Models<sup>b</sup> for F148W Image

Fit No.	Bulge	Nuclear Bulge <sup>c</sup>	Nucleus	$\chi^2$	No. of Parameters	Nucleus Mask
1	Sérsic	...	...	685,595	14	yes
2	Two Sérsic	...	...	673,491	21	yes
3	Three Sérsic	...	...	670,346	28	yes
4	Four Sérsic	...	...	668,586	35	yes
5	Three Sérsic	...	PSF	676,565	31	no
6	Sérsic	Sérsic ( $R_e = 5.8, n = 0.44$ )	...	690,714	19	no
7	Two Sérsic	Sérsic ( $R_e = 5.8, n = 0.44$ )	...	678,220	26	no
9	Sérsic	Sérsic ( $R_e = 5.8, n = 0.44$ )	PSF	689,436	22	no
10	Two Sérsic	Sérsic ( $R_e = 5.8, n = 0.44$ )	PSF	676,810	29	no
11	Three Sérsic	Sérsic ( $R_e = 5.8, n = 0.44$ )	PSF	674,513	36	no
12	Four Sérsic	Sérsic ( $R_e = 5.8, n = 0.44$ )	PSF	672,310	43	no

#### Notes.

<sup>a</sup> All fits include the dust mask, background, and three brightest stars. Bulge-only models are the top four rows and exclude the nuclear region.

<sup>b</sup> Rows 5–12 include whole image fitting. Row 5 is model for bulge plus compact nucleus, rows 6–8 are models for bulge plus nuclear bulge, and rows 9–12 are models for bulge plus nuclear bulge plus compact nucleus.

<sup>c</sup> Nuclear bulge Sérsic model has effective radius  $R_e$  and index  $n$  fixed to the values from Peng (2002).

the nucleus mask) of increasing complexity. Table 6 shows the results (rows 1–4) for the bulge modeled using one to four Sérsic functions, with each Sérsic component having seven free parameters. The decreases in  $\chi^2$  by adding the second, third, and fourth Sérsic functions are  $\simeq 12,000$ ,  $\simeq 3100$ , and  $\simeq 1800$ , respectively. These decreases are highly significant for the addition of seven extra parameters for each comparison: for example, extrapolating from the table on page 815 of Press et al. (1992), for seven parameters of interest, a  $3\sigma$  confidence level occurs for a decrease in  $\chi^2$  of 22.1, much less than the obtained decreases.

The maximum number of components we use for modeling the bulge without the nuclear region is four. The four-component fit (row 4) of Table 6 gives the best fit of the series that we used. It is better than the three-Sérsic fit (row 3) with a  $\chi^2$  smaller by 1760 for seven extra parameters, which is highly significant (Press et al. 1992). We could have added additional components beyond four before including the central nuclear region. Because the next step is fitting the bulge including the nuclear region, we redo the four-component model and then proceed with adding more functions in the next section below, rather than adding more functions for the fits without the nuclear region. Inclusion of the central part of image (the nuclear region) in the fits helps to obtain more realistic parameters of the components for the bulge and is essential to determine the components for the nuclear region.

### 3.2. Model for the Bulge with Nuclear Region

M31 has a complex nuclear and bulge morphology, so a simple radial luminosity profile is not a sufficient model. When fitting the M31 double nucleus using high-resolution HST data, Peng (2002) identified four nucleus components: a UV peak, the dynamic center, and two other focal points known as P1 and P2 in the literature. That work adds a nuclear bulge component to complete the model for the light distribution. In total Peng (2002) used six components to achieve an optimal fit.

#### 3.2.1. Bulge plus Nuclear Region Model with Fixed Nuclear Parameters

For these fits, the Sérsic function for the nuclear bulge has effective radius  $R_e$  and index  $n$  fixed to the values from Peng (2002). We use a PSF function for the compact nucleus because it is unresolved with UVIT, although it is complex at the subarcsecond scale (Peng 2002). Table 6 shows results (rows 5–12) for model fits including the nuclear region (no nucleus mask). These use various numbers of Sérsic functions for the bulge, plus one Sérsic for the nuclear bulge and a PSF function for the compact nucleus.

Comparing the different models in Table 6, we find the following. First, we compare fits for the bulge only (rows 1–3 in Table 6) with the fits including nucleus (row 5) or nuclear bulge (rows 6–8), with the nuclear bulge parameters fixed to

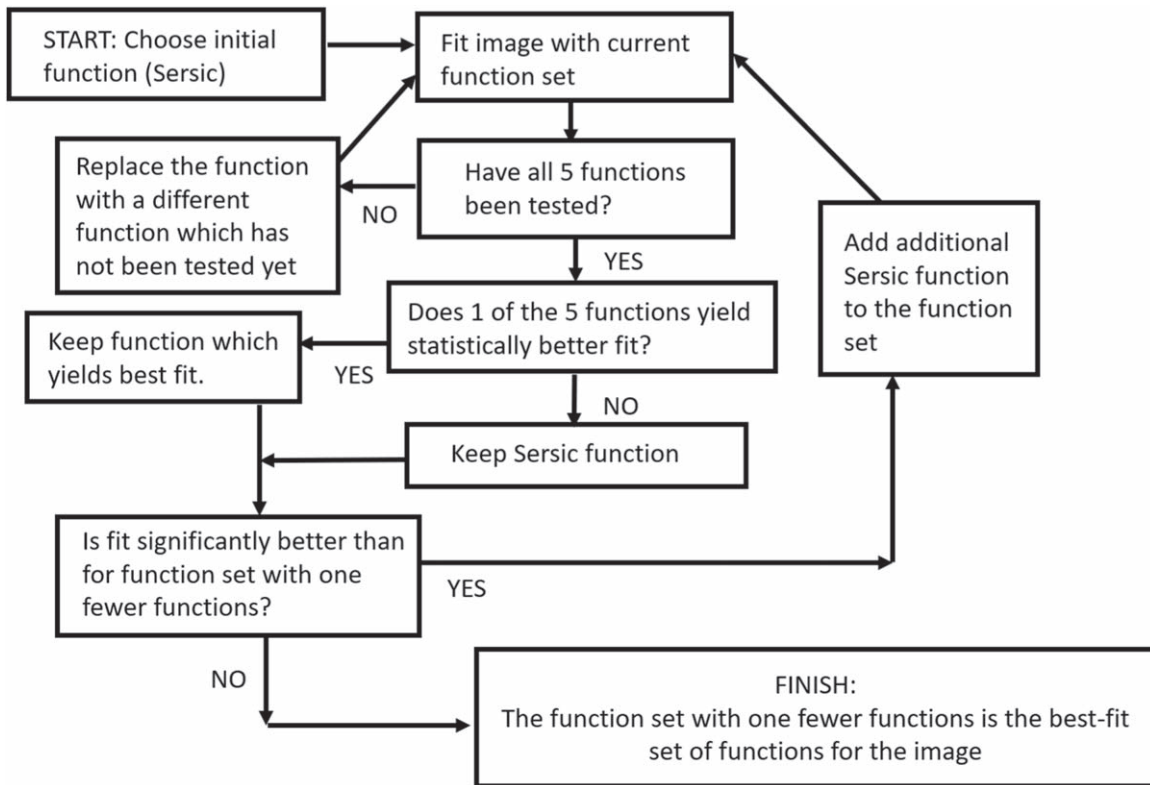


Figure 2. Flowchart for finding best-fit set of functions to the image of the M31 bulge (Sections 2.2.1 and 3.2.2).

the (Peng 2002) values, except normalization. For fits including the pixel mask, the degrees of freedom (dof) is reduced by 1681, from  $1,002,001 - N_{\text{par}}$  to  $1,000,320 - N_{\text{par}}$ . The three-Sérsic plus PSF fit (row 5) for the bulge plus nuclear region (with 1681 more pixels than the bulge with nuclear mask) has higher  $\chi^2$  by  $\sim 6200$  than the three-Sérsic fit for the bulge alone (row 3). This is significantly higher than the expected increase of 1681, the extra dof introduced by including the  $41 \times 41$  pixel nuclear region. This shows that the PSF alone does not provide a good fit to the nuclear region. Similarly, comparison of row 1 with row 6, row 2 with row 7, or 3 with row 8 shows increases of  $\chi^2$  of  $\simeq 5000$  for each case. This is much higher than the extra dof introduced, showing that the nuclear bulge with fixed parameters does not provide a better fit.

Next, we compare fits to the bulge only (rows 1–4) with fits including bulge, nucleus, and nuclear bulge (rows 9–12). The one, two, three, and four Sérsic bulge fits with nucleus and nuclear bulge have increases in  $\chi^2$  of 3841, 3319, 4167, and 3724, respectively, over fits without nucleus and nuclear bulge. This is much greater than the extra dof introduced. We conclude that the model with fixed parameter Sérsic plus PSF is not a good model for the nuclear region (nucleus plus nuclear bulge).

### 3.2.2. Bulge plus Nuclear Region Model with Free Nuclear Parameters

For our final set of fits to the bulge plus nuclear region, we use models for the compact nucleus plus nuclear bulge, with nuclear model parameters not tied to the values from Peng (2002). The nuclear region observed by UVIT in the F148W filter has lower resolution than the HST F555W data, and the wavelength is significantly different, so different stars are

prominent in F148W than in the HST data. The F148W filter extends from 125 to 175 nm (Tandon et al. 2017), so the bulge and nuclear region structure can be quite different than what was found at 555 nm by Peng (2002).

The procedure for finding the best-fit model, without fitting beyond what is statistically significant, is outlined in Figure 2. We start with a single function to model the bulge, including the nuclear region, and compare it to fits with the other four functions (see Section 2.2.1). The function with the best fit is chosen, and then the complexity is increased by adding an additional function to the function set. All five functions are tested as the added function, and the function set with the best fit was kept. Next, we test whether the current function set has a significantly better fit than the best fit with the function set with one fewer function. If yes, then we test a function set with one additional function, as shown in the flowchart. If not, the added function is not justified by the data, and the set with one fewer function is the final best-fit function set.

Models with free bulge and nuclear parameters with four to eight components are shown in Table 7, with parameter values and  $\chi^2$  values given. The model with nine components does not yield a statistically better fit and so is not shown. Neither do we show the models with three or fewer components, as these are inadequate to fit the bulge plus nuclear region and have significantly worse fits. The parameter errors are those generated by GALFIT from the fitting process.

We compare the models to comparable models with fixed nuclear parameters, shown in Table 6. Model 1 in Table 7 has a lower  $\chi^2$  by 2479 than Model 8 from Table 6 but only two more parameters, thus a significantly better fit. Comparing Model 1 in Table 7 with Model 11 from Table 6 yields that Model 1 in Table 7 has a lower  $\chi^2$  by 1268 with one less



**Table 7**  
Comparison of Parameters for Models<sup>a</sup> with Four or More Components for Bulge plus Nuclear Bulge/Nucleus for F148W Image

Model	Comp.	Center Offset (arcseconds)	Magnitude	$R_e$ (arcseconds or kpc) <sup>b</sup>	Sérsic Index	FWHM (arcseconds or kpc) <sup>b</sup>	Power Law	Axis Ratio	Position Angle <sup>b</sup> (deg)
1: four components Parameter No.: 35 $\chi^2$ : 673,245	Bulge								
	Sérsic	$41.56 \pm 0.23$	$12.78 \pm 0.12$	$393 \pm 29$ ( $1.50 \pm 0.11$ )	$1.12 \pm 0.04$			$0.620 \pm 0.003$	$-46.2 \pm 0.5$
	Sérsic	$0.76 \pm 0.02$	$13.30 \pm 0.02$	$86.2 \pm 1.0$ ( $0.328 \pm 0.038$ )	$1.48 \pm 0.01$			$0.760 \pm 0.001$	$-58.1 \pm 0.1$
	Sérsic	$16.84 \pm 0.71$	$14.67 \pm 0.02$	$196.6 \pm 2.9$ ( $0.748 \pm 0.011$ )	$0.30 \pm 0.01$			$0.760 \pm 0.001$	$-58.1 \pm 0.1$
	Nucleus Sérsic	$0.042 \pm 0.007$	$17.86 \pm 0.01$	$2.42$ (0.009)	$1.87 \pm 0.04$			$1.00 \pm 0.01$	n/a
2: five components Parameter No.: 41 $\chi^2$ : 672,430	Bulge								
	Sérsic	$41.73 \pm 0.20$	$12.78 \pm 0.12$	$393 \pm 29$ ( $1.50 \pm 0.11$ )	$1.12 \pm 0.03$				
	Sérsic	$0.84 \pm 0.02$	$13.30 \pm 0.02$	$86.2 \pm 1.0$ ( $0.328 \pm 0.038$ )	$1.48 \pm 0.01$			$0.770 \pm 0.001$	$-58.4 \pm 0.1$
	Sérsic	$16.59 \pm 0.70$	$14.67 \pm 0.02$	$196.6 \pm 2.9$ ( $0.748 \pm 0.011$ )	$0.30 \pm 0.01$				
	Nucleus Moffat Gaussian	$0.28 \pm 0.03$ $0.023 \pm 0.008$	$18.07 \pm 0.02$ $19.00 \pm 0.01$			$11.1 \pm 2.3$ ( $0.042 \pm 0.009$ ) $2.22 \pm 0.04$ ( $0.0084 \pm 0.0002$ )	$8.8 \pm 3.0$	$0.70 \pm 0.01$ $0.80 \pm 0.02$	$-34.7 \pm 1.0$ $-34.7 \pm 1.0$
3: six components Parameter No.: 48 $\chi^2$ : 671,077	Bulge								
	Sérsic	$42.88 \pm 0.20$	$12.78 \pm 0.12$	$393 \pm 29$ ( $1.50 \pm 0.11$ )	$1.12 \pm 0.035$			$0.63 \pm 0.01$	$-46.9 \pm 0.5$
	Sérsic	$.98 \pm 0.01$	$13.30 \pm 0.02$	$86.2 \pm 1.0$ ( $0.328 \pm 0.038$ )	$1.48 \pm 0.01$			$0.77 \pm 0.01$	$-60.7 \pm 0.1$
	Sérsic	$16.97 \pm 0.71$	$14.67 \pm 0.019$	$196.6 \pm 2.9$ ( $0.748 \pm 0.011$ )	$0.30 \pm 0.01$			$0.42 \pm 0.01$	$-47.4 \pm 0.2$
	Nucleus Moffat Moffat Gaussian	$0.46 \pm 0.049$ $12.51 \pm 0.15$ $0.028 \pm 0.008$	$18.06 \pm 0.019$ $18.74 \pm 0.028$ $19.03 \pm 0.01$			$25.1 \pm 4.9$ ( $0.095 \pm 0.018$ ) $32 \pm 27$ ( $0.122 \pm 0.102$ ) $2.20 \pm 0.04$ ( $0.0084 \pm 0.0002$ )	$7.87 \pm 2.6$ $20.00 \pm 32$	$0.71 \pm 0.0063$ $0.46 \pm 0.011$ $0.77 \pm 0.02$	$-38.8 \pm 0.8$ $-9.9 \pm 0.9$ $-73.2 \pm 3.1$
4: seven components Parameter No.: 54 $\chi^2$ : 670,954	Bulge								
	Sérsic	$42.89 \pm 0.22$	$12.78 \pm 0.12$	$393 \pm 29$ ( $1.50 \pm 0.11$ )	$1.12 \pm 0.035$			$0.63 \pm 0.0025$	$-46.85 \pm 0.45$
	Sérsic	$0.9975 \pm 0.015$	$13.30 \pm 0.015$	$86.2 \pm 1.0$ ( $0.328 \pm 0.004$ )	$1.48 \pm 0.011$			$0.77 \pm 0.01$	$-60.7 \pm 0.1$
	Sérsic	$16.97 \pm 0.71$	$14.67 \pm 0.019$	$196.6 \pm 2.9$ ( $0.748 \pm 0.011$ )	$0.30 \pm 0.0058$			$0.42 \pm 0.0013$	$-47.41 \pm 0.19$
	Nucleus Moffat Moffat Gaussian	$0.154 \pm 0.010$ $12.69 \pm 0.05$ $0.112 \pm 0.024$	$18.11 \pm 0.019$ $18.74 \pm 0.029$ $19.41 \pm 0.047$			$11.5 \pm 3.6$ ( $0.044 \pm 0.014$ ) $30 \pm 25$ ( $0.114 \pm 0.095$ ) $1.88 \pm 0.04$ ( $0.0072 \pm 0.0002$ )	$12.27 \pm 6.9$ $20.00 \pm 32$	$0.67 \pm 0.0072$ $0.51 \pm 0.013$ $0.71 \pm 0.023$	$-37.4 \pm 1.1$ $-9.70 \pm 1.5$ $-48.4 \pm 5.8$
	Gaussian	$0.28 \pm 0.15$	$19.95 \pm 0.071$			$4.34 \pm 0.27$ ( $0.0165 \pm 0.0010$ )		$0.38 \pm 0.021$	$86.0 \pm 1.9$

**Table 7**  
(Continued)

Model	Comp.	Center Offset (arcseconds)	Magnitude	$R_e$ (arcseconds or kpc) <sup>b</sup>	Sérsic Index	FWHM (arcseconds or kpc) <sup>b</sup>	Power Law	Axis Ratio	Position Angle <sup>b</sup> (deg)
5: eight components	Bulge								
Parameter No.: 59 $\chi^2$ : 670,885	Sérsic	$42.95 \pm 0.20$	$12.78 \pm 0.12$	$393 \pm 29$ ( $1.50 \pm 0.11$ )	$1.12 \pm 0.035$			$0.63 \pm 0.0025$	$-46.8 \pm 0.5$
	Sérsic	$0.988 \pm 0.015$	$13.30 \pm 0.015$	$86.2 \pm 1.0$ ( $0.328 \pm 0.038$ )	$1.48 \pm 0.011$			$0.77 \pm 0.0008$	$-60.8 \pm 0.1$
	Sérsic	$17.02 \pm 0.71$	$14.67 \pm 0.019$	$196.6 \pm 2.9$ ( $0.748 \pm 0.011$ )	$0.30 \pm 0.0058$			$0.42 \pm 0.0013$	$-47.4 \pm 0.2$
	Nucleus								
	Gaussian	$0.075 \pm 0.028$	$18.17 \pm 0.0096$			$11.73 \pm 0.14$ ( $0.0446 \pm 0.0005$ )		$0.71 \pm 0.0076$	$-38.9 \pm 1.0$
	Gaussian	$12.58 \pm 0.16$	$18.71 \pm 0.027$			$30.7 \pm 1.0$ ( $0.117 \pm 0.004$ )		$0.52 \pm 0.016$	$-9.3 \pm 1.2$
	Gaussian	$0.104 \pm 0.009$	$19.30 \pm 0.038$			$2.01 \pm 0.04$ ( $0.0077 \pm 0.0002$ )		$0.71 \pm 0.020$	$-49.4 \pm 5.3$
	Gaussian	$0.32 \pm 0.06$	$20.04 \pm 0.083$			$4.51 \pm 0.28$ ( $0.017 \pm 0.001$ )		$0.38 \pm 0.021$	$86.3 \pm 2.1$
Sérsic	$3.18 \pm 0.16$	$21.95 \pm 0.12$	$5.8$ (0.022)	$0.24$			$0.44 \pm 0.0$	$-2.4 \pm 1.5$	

**Note.**

<sup>a</sup> All fits include the dust mask, background, and three brightest stars.

<sup>b</sup> Position angle is counterclockwise from  $N$ .  $R_e$  in kiloparsecs is given in parentheses.

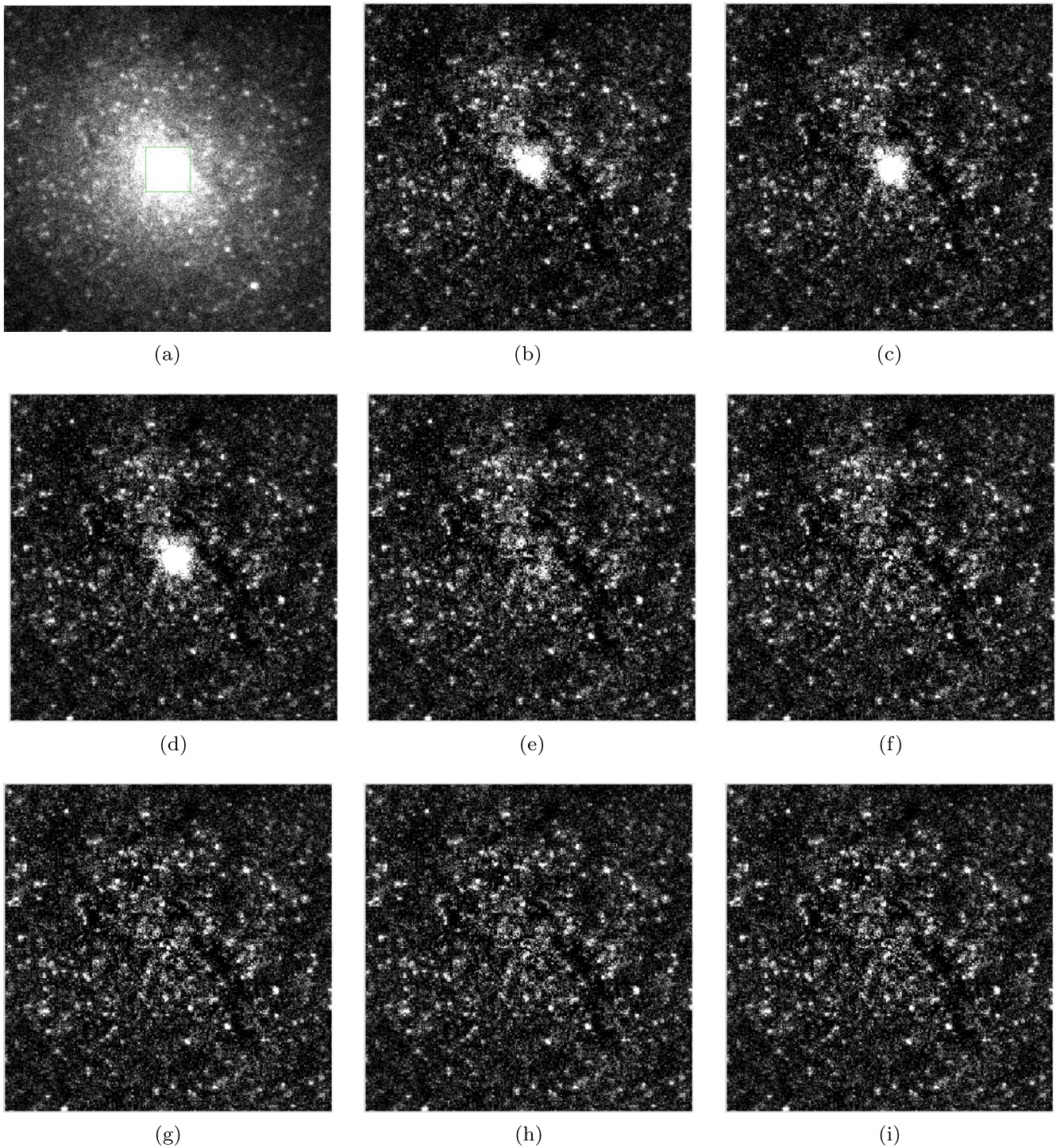


**Figure 3.** Central part of F148W image (a) and residual images for a series of models (b)–(i). Each image is  $125'' \times 125''$  ( $475 \text{ pc} \times 475 \text{ pc}$ ) centered on the nucleus. The gray scale for each image scale is linear from the image mean  $-0.5$  standard deviations to the image mean  $+5$  standard deviations. Panel (a) shows the nuclear region excluded (green rectangle) for the bulge-only fits (b), (c), and (d). Panels (b), (c), and (d) show the residual images for the best one-, two-, and three-component fits for the bulge with nuclear region excluded. These are the one-, two-, and three-Sérsic models with Sérsic index free and that have  $\chi^2$  and parameters given in Tables 4 and 5. Panels (e)–(i) show the residual images for the best four-, five-, six-, seven-, and eight-component fits for the bulge including the nuclear region. These models are given in Table 7. The residual images are given in order of decreasing  $\chi^2$  for each set ((b)–(d) fits with nuclear region omitted, and (e)–(i) fits to the entire image).

parameter. Thus, we conclude that the free nuclear region parameters result in much better fits and that the nucleus shape for the 148 nm image is significantly different than for 555 nm.

We next compare the different models in Table 7. The models with more components (and thus parameters) generally have lower  $\chi^2$ . The  $\Delta\chi^2$  values are compared here to determine

how much better are the more complex models. Model 2, with 41 parameters, has  $\Delta\chi^2 = 815$  compared to model 1, with six extra parameters. This is a highly significant improvement in fit (Press et al. 1992). Model 3 has  $\Delta\chi^2 = 1351$  compared to model 2, with seven extra parameters, again a highly significant improvement in the fit. Model 4 has  $\Delta\chi^2 = 123$  compared to

model 3, with six extra parameters. This is a significant improvement in the fit.<sup>8</sup> Model 5 has  $\Delta\chi^2 = 69$  compared to model 4, with five extra parameters, which is a significant improvement in fit. We did not proceed with more complex models than Model 5 for two reasons: the improvement in fit was no longer highly significant, and GALFIT would not converge from almost all the models attempted, likely because the number of parameters was too large. Thus, our final model for the bulge and nuclear region is Model 5 with three components for the bulge and five components for the nuclear region.

Residual images are obtained by subtracting model images from the original image. Figure 3 illustrates the process of finding the best combination of functions for the bulge of M31. It shows the original F148W observed image (top left) and, in the remaining panels, residual images for successively better models for the central  $125'' \times 125''$  ( $475 \text{ pc} \times 475 \text{ pc}$ ) region centered on the M31 compact nucleus.

The best-fit  $\chi^2$  values are successively lower for the residual images in successive panels. The second panel in the top row is for a single-Sérsic model for the bulge and no nuclear model (row 1 in Table 6). The single-Sérsic model, although it accounts for the bulk of the light from the bulge (in comparison with the first panel), has a significant residual in the nuclear region (inner  $41 \times 41$  pixel region) and thus does not fit the light distribution of bulge plus nuclear region. Successive models (residuals in panels 3 and 4, for the two-Sérsic and three-Sérsic models) fit the region outside the  $41 \times 41$  pixel nuclear region and represent the structure of the outer region more accurately, but they do not fit the nuclear region. Panels 5–9 are for models 1–5 in Table 7, which include components for the nuclear region. These show increasingly better fits (smaller residuals) in the nuclear region while maintaining or improving the fit to the outer region. The last panel in the bottom row is for our final bulge plus nuclear region model 5 with eight components shown in Table 7. This model yields no visible artifacts in the nuclear region at the center or in the bulge farther out.

From the residual images in Figure 3, it is seen that as the fit improves, the residuals in the nuclear region decrease. The final model fits well the large-scale structure of the bulge and the smaller-scale structure of the nuclear bulge and nucleus. There remains significant small-scale structure in the last image shown. The residual structures that are not modeled are seen to consist primarily of dust lanes and a number of small (few arcseconds across) bright spots scattered throughout the region.

### 3.3. Bulge/Nucleus Offset and Model Asymmetry

Because the components of the multicomponent models have different centers, axis ratios, and position angles, the total model is expected to have some asymmetry. We find that to be the case, as illustrated in Figure 4(a) for the best-fit eight-component model from Table 7. The centers of each component, in general, are offset from the position of the M31 nucleus (Peng 2002). The model components for the nucleus (compact nucleus plus nuclear bulge) have low offsets. From Table 7 the eight-component model has nucleus component offsets from  $\simeq 0''.08$  to  $12''.6$ , with only the most extended component (the second Gaussian) having an offset

exceeding  $3''.2$ . Higher offsets occur for the centers of the bulge model functions. Generally the three Sérsic components for the bulge (see Table 7) have offsets of  $\sim 42''$ ,  $\sim 1''$ , and  $\sim 16''$ . The offsets as a fraction of the  $R_e$  values are  $\sim 0.1$ ,  $\sim 0.01$ , and  $\sim 0.08$ , respectively.

The M31 bulge model (sum of all components; Figure 4(a)) exhibits an asymmetry in the bulge light distribution, consistent with the fractional offsets ( $\sim 0.1$ ) listed above for the centers of the model components. The model has deviation from perfect elliptical symmetry and shows a faint extension to the NNW of the center of the bulge. We illustrate how the individual components contribute to the shape and asymmetry of the bulge: panel (b) shows the three large bulge model Sérsics by their ellipses with semimajor axes  $R_e$ , including orientation and offsets; panel (c) shows the nuclear region model with the four Gaussian plus Sérsic components. The asymmetry and NNW extension are also seen in the original observation (Figure 1(a)); however, in the data the extra confusion caused by the clumpiness of the bulge makes it more difficult to discern. A large number of components (eight in the final model) are needed in order to produce a good fit to the asymmetry and NNW extension. Thus, to a large extent it is a phenomenological model for a light distribution that differs from an elliptical Sérsic distribution. The meaning of the different components used to fit the bulge is discussed further in Section 4.3.

## 4. Discussion

### 4.1. The Choice of GALFIT for Image Fitting

GALFIT's performance has been tested in fitting brightness distributions of galaxies. Simmons & Urry (2008) used a sample of 50,000 simulated galaxies to find that GALFIT returned the Sérsic index correctly for more than 90% of the cases. Price et al. (2017) tested the recovery of galaxy sizes with GALFIT and found only small offsets between for both star-forming and quiescent galaxies. Häußler et al. (2013) tested GALFIT on simulated data and found recovery of parameters, including magnitude. Using simulating galaxies from the Sloan Digital Sky Survey, Meert et al. (2013) find that single-Sérsic function parameters are recovered with  $\sigma_{\text{mag}} \approx 0.025 \text{ mag}$  and  $\sigma_{\text{radius}} \approx 5\%$ . Häußler et al. (2007) and Häußler et al. (2008) used simulated galaxies to test the performance of GALFIT against GIM2D, another two-dimensional fitting algorithm. Their results suggest that GALFIT outperforms its counterpart in almost all of the tested categories. The performance tests conducted over the years on GALFIT have established it as a benchmark software for two-dimensional galaxy modeling.

New fitting algorithms that are designed on neural network and deep-learning computational principles frequently use GALFIT to test their software. For example, Tuccillo et al. (2018) use deep neural networks to study galaxy morphology and show that their new algorithm produces results as good as GALFIT but much faster.

### 4.2. Comparison of Single-Sérsic Fits with Previous Model Fits of the M31 Bulge

The other UVIT filter images (F169M, F172M, N219M, and N279N) for the M31 bulge region (inner  $\simeq 1.59 \text{ kpc} \times 1.59 \text{ kpc}$ ) were fit with single-Sérsic functions. The small central nuclear region is omitted for these fits. The resulting single-

<sup>8</sup>  $\Delta\chi^2 = 20.1$  is a  $3\sigma$  improvement for six parameters, from Press et al. (1992).

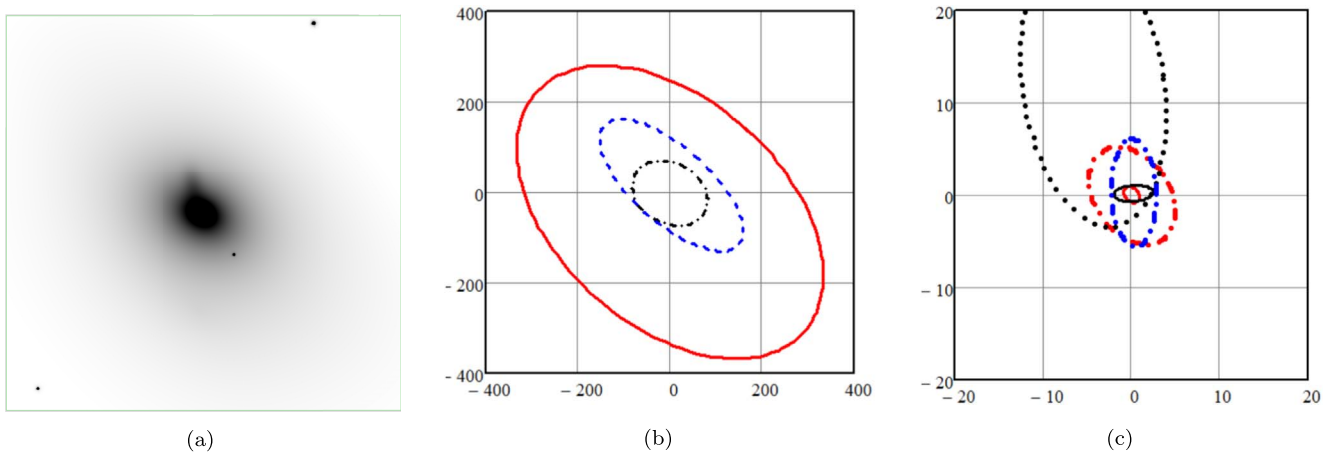


**Figure 4.** (a) Full ( $417'' \times 417''$ ) image of the eight-component bulge model (listed in Table 7). (b) Large ( $800'' \times 800''$ ) region showing the ellipses with semimajor axis  $R_e$  for the three Sérsic components of the bulge model. (c) Central ( $40'' \times 40''$ ) region showing the ellipses with semimajor axis FWHM/2 for Gaussians or  $R_e$  for the five components of the nuclear region model. Panels (b) and (c) have different scales than panel (a) in order to show the components with their greatly different sizes.

**Table 8**  
One-component Sérsic Parameters for the Five UVIT Images

Image	Component	Magnitude	$R_e$ (arcseconds or kpc) <sup>a</sup>	Sérsic Index	Axis Ratio	Position Angle (deg)
F148W	Sérsic	$11.78 \pm 0.02$	$127 \pm 3$ ( $0.483 \pm 0.011$ )	$2.52 \pm 0.02$	$0.730 \pm 0.001$	$-48.3 \pm 0.1$
F169M	Sérsic	$12.43 \pm 0.05$	$120 \pm 6$ ( $0.457 \pm 0.023$ )	$2.51 \pm 0.05$	$0.740 \pm 0.002$	$-48.1 \pm 0.3$
F172M	Sérsic	$13.30 \pm 0.06$	$134 \pm 8$ ( $0.510 \pm 0.030$ )	$2.66 \pm 0.07$	$0.750 \pm 0.002$	$-48.3 \pm 0.3$
N219M	Sérsic	$12.05 \pm 0.09$	$176 \pm 15$ ( $0.670 \pm 0.057$ )	$2.52 \pm 0.08$	$0.770 \pm 0.002$	$-48.2 \pm 0.4$
N279N	Sérsic	$11.04 \pm 0.06$	$144 \pm 8$ ( $0.548 \pm 0.030$ )	$2.14 \pm 0.05$	$0.750 \pm 0.002$	$-48.1 \pm 0.3$

**Note.**

<sup>a</sup>  $R_e$  in kiloparsecs is given in parentheses.

Sérsic fit parameters, including the F148W fit, are given in Table 8. The Sérsic indices range from  $n = 2.14 \pm 0.05$  at 279 nm to  $n = 2.51$  to 2.66 for the 148–219 nm data, the effective radii are  $R_e = 0.46$ –0.51 kpc, and the ellipticities are  $\epsilon = 1 - q = 0.25$ –0.27.

A number of previous works have studied the structural properties of M31, including the bulge. Seigar et al. (2008) fit the Spitzer 3.6  $\mu\text{m}$  1D profile with a Sérsic bulge plus and exponential disk, finding Sérsic index  $n = 1.71 \pm 0.11$  and  $R_e = 1.93$  kpc. Courteau et al. (2011) fit both minor- and major-axis profiles combining the infrared data (either Spitzer 3.6  $\mu\text{m}$  or  $I$ -band (0.9  $\mu\text{m}$ ) data from Choi et al. 2002) with star count data added for the outer regions. They find (their Table 2) Sérsic indices between  $n = 2.0$  and 2.6 for the major axis with  $R_e = 0.8$ –1.2 kpc, with both ranges including uncertainties. For the minor axis, they find Sérsic indices between  $n = 1.7$  and 2.4 with  $R_e = 0.2$ –0.8 kpc. Combined minor- and major-axis fits yield Sérsic index  $n = 2.18 \pm 0.06$  with  $R_e = 0.82 \pm 0.04$  kpc and ellipticity  $\epsilon = 0.28 \pm 0.01$  for the Spitzer data and Sérsic index  $n = 1.83 \pm 0.04$  with  $R_e = 0.74 \pm 0.02$  kpc and  $\epsilon = 0.28 \pm 0.01$  for the Choi et al. (2002) data. Thus, wide ranges of Sérsic index,  $R_e$ , and  $\epsilon$  are found, depending on the data used and on the fitting method.

Dorman et al. (2013) analyze the  $I$ -band data from Choi et al. (2002) combined with star data (counts and kinematics) to fit structural parameters, luminosity functions, and disk fractions (based on kinematics). They find (their Table 2) a Sérsic index  $n = 1.92 \pm 0.08$  and  $R_e = 0.78 \pm 0.03$  kpc for the bulge, with ellipticity  $\epsilon = 0.28 \pm 0.01$ . This confirms these values for the  $I$  band, consistent with Courteau et al. (2011), which are

different (smaller  $n$  and  $R_e$  and larger  $\epsilon$ ) than values derived using 3.6  $\mu\text{m}$  data.

In summary, previous works in  $I$  band and 3.6  $\mu\text{m}$  yield single-Sérsic fits to the bulge with Sérsic indices from 1.7 to 2.6, with most errors  $\sim 0.05$ –0.2, and major axis  $R_e$  from 0.7 to 1.9 kpc, with most errors  $\sim 0.01$ –0.1. Fits including both major and minor axes find  $\epsilon = 0.21$ –0.28, with error 0.01. The UVIT FUV and NUV results are not so different: the UVIT single-Sérsic indices are higher except for the N279N filter, the  $R_e$  values are smaller, and the  $\epsilon$  values are the same as the  $I$ - and 3.6  $\mu\text{m}$  band values. The differences are not surprising given the difference in wave band: cooler stars are more prominent in  $I$  and 3.6  $\mu\text{m}$  bands, whereas hot stars are more prominent in the NUV and FUV bands. Hot star emission has a major contribution from extreme horizontal branch stars, post-AGB stars, post-early AGB stars, and AGB-manque stars (Rosenfield et al. 2012), which are likely distributed differently than the cool stars.

### 4.3. Interpretation of Multicomponent Fits

In modeling the UVIT F148W image of the M31 bulge, we carried out a series of tests. The dust lanes have a significant effect and so were masked (not included) in the fits (Section 2.2.4). Several bright stars affect the fits and so are included separately (Section 2.2.5). The nuclear region is a separate component, so when modeling the bulge only, the nuclear region is masked (Sections 2.2.6 and 3.1). Then, we fit the bulge with a single Sérsic function and multiple Sérsic functions. We carried out fits including the nuclear region (Section 3.2), with model functions for both the bulge and

nuclear region, where the nuclear region includes the compact nucleus plus the nuclear bulge (Peng 2002). The most relevant fits for comparison with previous work on models for the M31 bulge are the single-component Sérsic fits, listed in Table 8.

The purpose of the multicomponent fits to the bulge and nuclear region was to obtain a more accurate, although much more complex, functional description of the asymmetric surface brightness of the bulge and nuclear region. From Table 7, with three Sérsic components for the bulge and one to five components for the nuclear region, the FUV (F148W) light distribution is seen to be complex and better described by multiple components than a single component. These components are a purely phenomenological description of the F148W light distribution. They were derived from fitting the two-dimensional light distribution only, without constraints from other data, from simulations, or from theory.

The three Sérsic components for the F148W emission from the bulge, with different models for the nuclear region, consistently have  $R_e$  values of 0.33, 0.75, and 1.5 kpc and respective Sérsic indices of 1.1, 1.5, and 0.3. The three Sérsic functions have different axis ratios, different position angles, and different centers (by up to  $42''$  or 0.16 kpc for the Sérsic function with  $R_e = 1.5$  kpc) in order to fit the asymmetry in the light distribution of the bulge (see Figures 4(a) and (b)). For the bulge region, it is known to be complex from the work of Peng (2002) and references therein. The five-component model (model 5 in Table 7) for the nuclear region is illustrated in Figure 4(c). This fit is a phenomenological model for the complex FUV light distribution in the nuclear region. The fit was carried out simultaneously with the three-Sérsic model for the bulge in order to separate, as best as possible, the nuclear region light from the bulge region light in the nuclear region.

The M31 bulge light distributions in the other UVIT filters (F169M, F172M, N219M, and N279N) were fit with multicomponent models. The results of those fits are given in the Appendix and Table 10. With the lower S/N for those images, the number of components was 4, and the parameters of those components are considerably less well constrained.

#### 4.4. Bulge Type

##### 4.4.1. Discussion of Bulge Type

The two bulge categories of pseudobulges and of classical bulges are essential in understanding galaxy formation history (KK04; Fisher & Drory 2008). According to KK04, the Sérsic index can be used to classify bulges, or at least provide evidence in favor of one of the types in the absence of kinematic information. A Sérsic index value less than 2 is consistent with a pseudobulge, while classical bulges have a characteristic Sérsic index greater than 2 (KK04; Gadotti 2008; Fisher & Drory 2008, 2016). Athanassoula et al. (2016) distinguish (i) classical bulges by having a spheroidal shape, Sérsic index  $>2.5$ , and  $V_{\max}/\sigma$  values that are less than for isotropic oblate rotators; and (ii) pseudobulges by having the shape of a disk, Sérsic index  $<2.5$ , and clear signs of rotation.

Caon et al. (1993) demonstrated that ellipticals and galactic bulges are better fit if the exponent of the  $r^{1/4}$  term in the de Vaucouleurs formula is a free parameter as  $r^{1/n}$ , equivalent to the Sérsic function with index  $n$ . Further studies, such as Courteau et al. (1996), strengthened the idea that “late-type” bulges have a Sérsic index between 1 and 2. This led KK04 to

include  $n$  between  $\approx 1$  and 2 as one of the diagnostic tests for galactic pseudobulges. Fisher & Drory (2008) performed bulge–disk decompositions on a sample of spiral galaxies and likewise concluded that Sérsic indices smaller than 2 are indicative of a pseudobulge, while those greater than 2 are indicative of a classical bulge. This is confirmed by the Gadotti (2008) study on the structural parameters of bulges, bars, and disks. They found that bulges show significantly different parameters than ellipticals, with a greater dispersion for pseudobulges. Fisher & Drory (2010) find that values of  $n < 2$  may be interpreted as evidence of secular evolution in the bulge, and they suggest that their  $n$  value close to 2 suggests “some amount” of secular evolution. Nine S0–Sb galaxies that have two-component bulges (classical plus pseudobulge) are the subject of an observational study by Erwin et al. (2015). They find that the disk pseudobulges consist of an exponential disk with nuclear rings, nuclear bars, or spiral arms and that the classical bulge components have Sérsic indices in the range 0.9–2.2.

Simulations of galaxy evolution provide a guide to the structural differences between pseudobulges and classical bulges. Guedes et al. (2011) present a cosmological  $N$ -body hydrodynamic simulation in which the evolutionary pathway of a close analog to the Milky Way disk galaxy is studied. Bulge formation was observed to have occurred through slow secular processes by the interaction of the various structural components of the galaxy, rather than fast and energetic merger events, which were absent in the simulation. Their simulation outcome of a “present-day” disk shape with a complex structure showing nuclear, bulge, disk, and halo regions was subsequently subjected to a GALFIT decomposition. The resulting bulge Sérsic index was  $n = 1.4$ . Simulations for a major merger of two gas-rich pure disk galaxies (Keselman & Nusser 2012) find that the resulting bulge has Sérsic index  $\sim 0.3$ – $0.9$ . When the initial galaxies have gas halos (Athanassoula et al. 2016), the immediate outcome is a classical bulge, but a pseudobulge and a thin disk grow from gradually accreted gas, which can be considered secular evolution. The kinematics and range of stellar ages for the classical and pseudobulge are very different. The classical bulge (stars born at time  $t < 1.4$  Gyr) has a Sérsic index of  $n \sim 4$ – $6$ ; the four remaining components (stars born at time intervals  $1.4 \text{ Gyr} < t < 1.8 \text{ Gyr}$ ,  $1.8 \text{ Gyr} < t < 2.2 \text{ Gyr}$ ,  $2.2 \text{ Gyr} < t < 9 \text{ Gyr}$ , and  $9 \text{ Gyr} < t < 10 \text{ Gyr}$ ) can be fit with a combination of three exponential disks.

A second characteristic of pseudobulges as described by KK04, Courteau et al. (1996), and Fisher & Drory (2010) is the presence of boxiness. Bulges showing box-shaped isophotes are well established observationally and theoretically (Sandage 1961; de Vaucouleurs 1974). Boxy bulges are observed in about one-fifth of edge-on spiral galaxies (de Souza & Dos Anjos 1987; Lütticke et al. 2000; Laurikainen & Salo 2016). KK04 conclude that the detection of boxy bulge isophotes is sufficient for the identification of a pseudobulge. This stems from the connection boxy bulges seem to have with galactic bars: they appear to be created by the interaction of the bar with the disk, as secular evolutionary mechanisms slowly construct the boxy bulge out of disk material.

##### 4.4.2. M31’s Bulge

For M31, Courteau et al. (2011) use one-dimensional decomposition methods to model the bulge and obtain a Sérsic index  $n = 2.2 \pm 3$ . They measured a ratio of bulge scale length

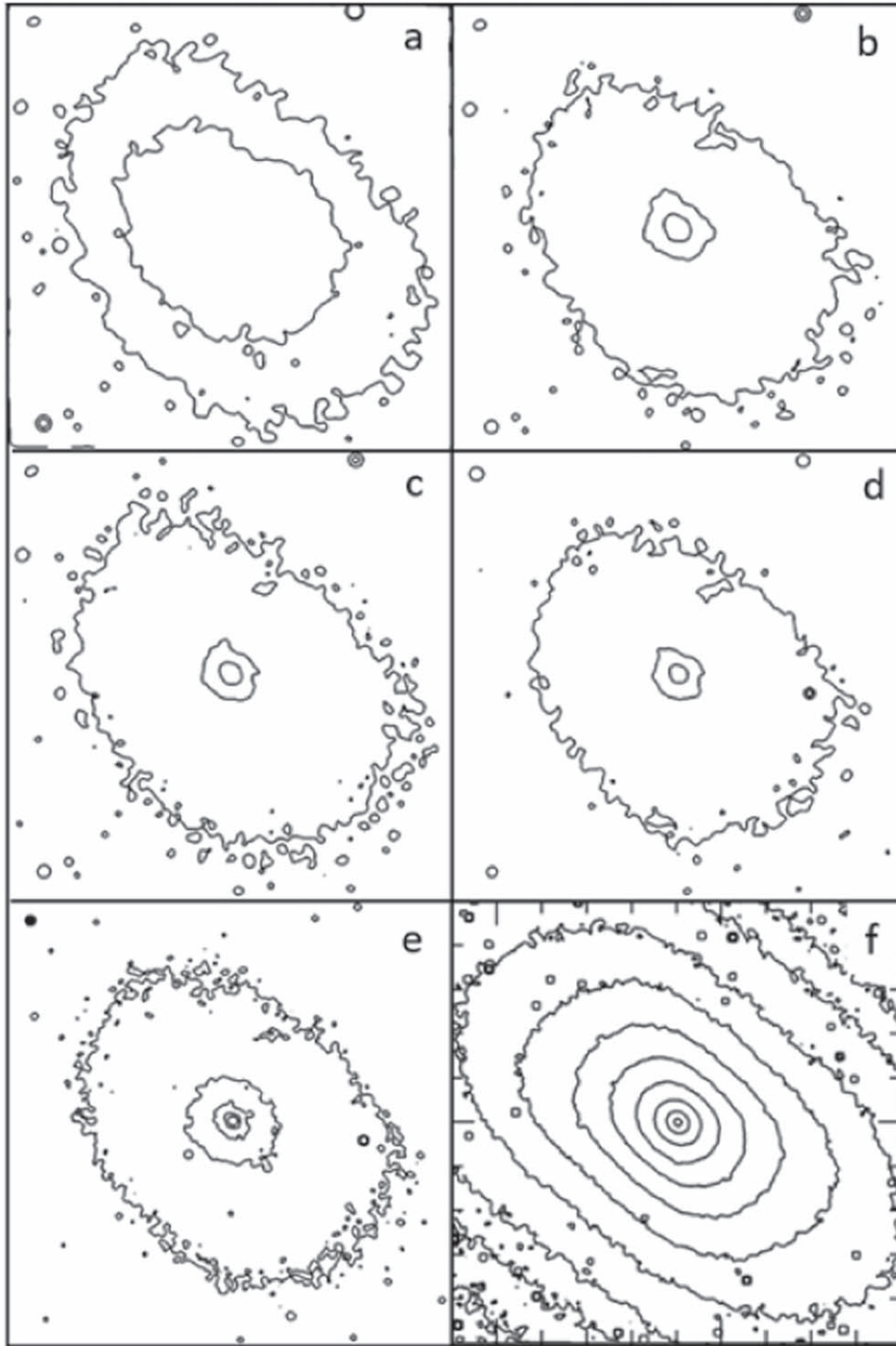


**Figure 5.** Contour lines for the UVIT images of the bulge of M31 in the (a) F148W, (b) F169M, (c) F172M, (d) N219M, and (e) N279N filters. On the same scale, the contours from Beaton et al. (2007) are shown for comparison in panel (f). The boxy nature of the contours is evident at all wave bands.

to disk scale length of 0.2, which agrees with the value of 0.2 that is obtained from secular evolution models (Courteau et al. 1996). Courteau et al. (2011) note that their Sérsic index is close enough to 2 to be consistent with some amount of secular evolution in the bulge, according to Courteau et al. (1996), Fisher & Drory (2010), and KK04. The study here shows that a single-Sérsic fit to the five UVIT images (Table 8) yields indices between  $\sim 2.1$  and  $\sim 2.6$ . Here we used two-dimensional image fitting with GALFIT, which should better model the light distribution than one-dimensional fits (see

Section 4.1). We obtain an M31 bulge Sérsic index of 2.14 for the 279 nm UVIT image, consistent with earlier results, and indices of  $\simeq 2.5$  for the four shorter-wavelength UVIT images (148–219 nm). The fact that the Sérsic index is  $\simeq 2$ – $2.5$  and neither clearly  $< 2$  nor clearly  $> 2.5$  indicates that there are probably contributions from a classical bulge and a pseudobulge in M31. The four shorter-wavelength images yield a larger Sérsic index, possibly indicating a smaller contribution from a pseudobulge relative to the classical bulge at shorter wavelengths.

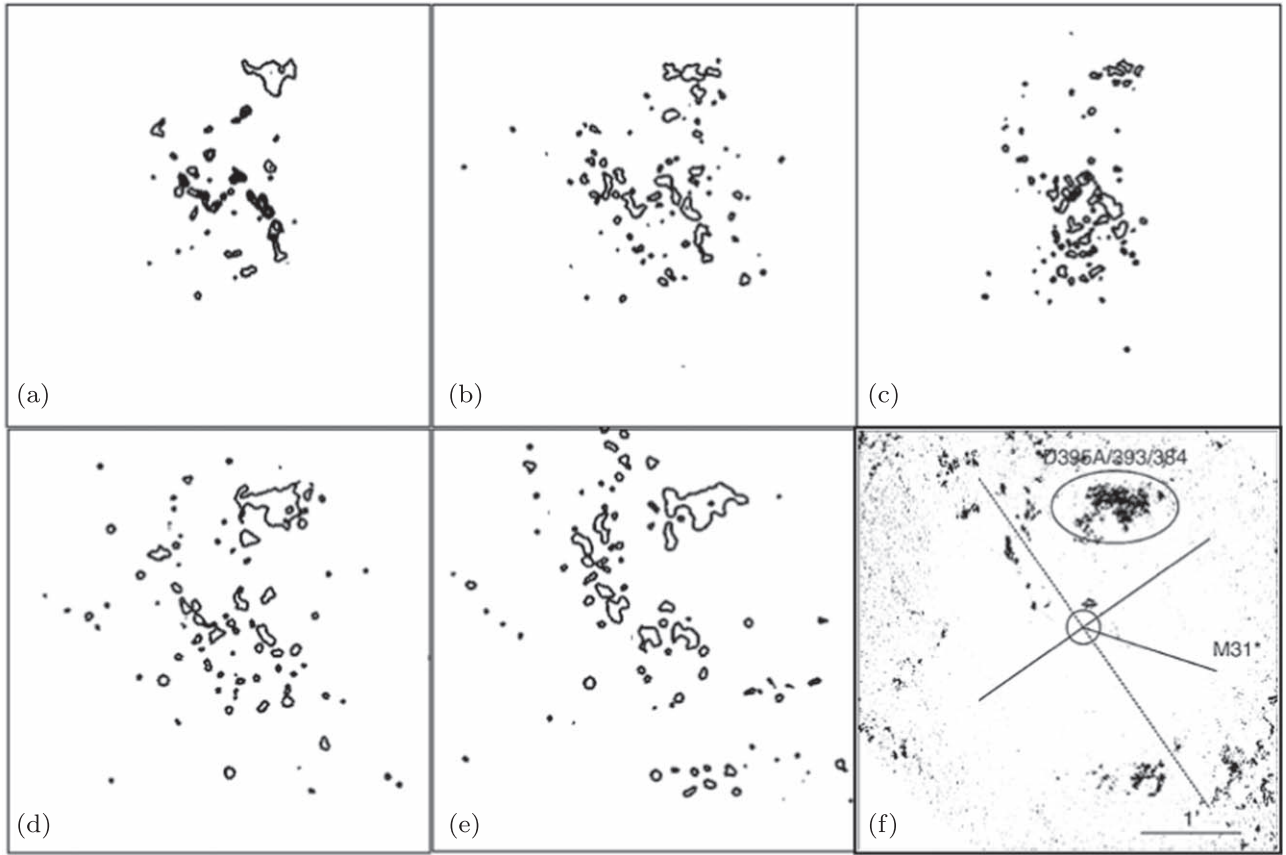


**Figure 6.** The nuclear spiral dust lane features: negative contours for the UVIT residual images (after subtraction of the best-fit bulge model) are shown in the first five panels: (a) F148W, (b) F169M, (c) F172M, (d) N219M, and (e) N279N; the extinction map from Dong et al. (2016) in gray scale is shown in panel (f). The ellipse in panel (f) marks a foreground dust cloud.

Several studies indicate that the M31 bulge is intrinsically an oblate spheroid with an axis ratio of  $\sim 0.8$  (Kent 1983; Widrow et al. 2003; Geehan et al. 2006), while others indicate a triaxial nature (Lindblad 1956; Stark 1977; Kent 1989; Stark & Binney 1994; Berman 2001; Berman & Loinard 2002). For both cases, two-dimensional fitting of the image is superior to one-dimensional fitting.

A near-infrared mapping study of M31 conducted by Beaton et al. (2007) revealed the boxy morphology of the bulge with high S/N and with little interference from dust extinction. The UVIT FUV and NUV images of the bulge of M31 show a boxy morphology. Figure 5 shows contour lines from the five UVIT images (panels (a)–(e)). Panel (f) shows the contour lines from Beaton et al. (2007), which illustrate similar boxiness to that seen in the N279N image in panel (e). The other UVIT filter images exhibit boxiness, although less strongly than that seen for the N279N image.

Most of the boxy or peanut-shaped features that have been reported in galaxies have been detected in infrared bands (Kormendy & Barentine 2010; Laurikainen & Salo 2016), such as Spitzer 3.6  $\mu\text{m}$  images. In the UV there have been no previous reports of bulge boxiness. However, all five of the UVIT filter images of the bulge of M31 show signs of a boxiness. Considering KK04’s third criterion, the bulge boxiness indicates a pseudobulge interpretation for M31’s bulge.

There are two ways to measure diskiness or boxiness from fitting images using GALFIT. The first method is the use of generalized ellipses instead of ellipses, as follows. The radial

**Table 9**  
Generalized Ellipse<sup>a</sup> ( $C_0$ ) and Fourier Mode 4<sup>b</sup> Measures of Boxiness

Image	$C_0$	$m = 4$ Fourier Mode Amplitude	Phase Angle (deg)
F148W	$0.193 \pm 0.007$	$0.0150 \pm 0.0006$	$-1.5 \pm 0.6$
F169M	$0.159 \pm 0.019$	$0.0124 \pm 0.0012$	$1.2 \pm 1.7$
F172M	$0.187 \pm 0.023$	$0.0144 \pm 0.0014$	$0.6 \pm 1.7$
N219M	$0.098 \pm 0.000$	$0.0085 \pm 0.0012$	$9.4 \pm 2.9$
N279N	$0.156 \pm 0.018$	$0.0121 \pm 0.0011$	$4.4 \pm 1.6$

**Notes.**

<sup>a</sup> Diskiness has  $C_0 < 0$ ; boxiness has  $C_0 > 0$ .

<sup>b</sup> The amplitude of the  $m = 4$  Fourier mode is  $>0$  for boxy ellipses and  $<0$  for disky ellipses.

functions are elliptical in shape, accomplished by making the radial coordinate  $r$  constant on ellipses, defined by

$$r(x, y) = \left( |x - x_c|^2 + \left| \frac{y - y_c}{q} \right|^2 \right)^{\frac{1}{2}}. \quad (6)$$

To allow the ellipse to have arbitrary orientation,  $(x, y)$  are rotated coordinates. To change this into generalized boxy or peanut-shaped ellipses, the power is changed from 2 to  $C_0 + 2$  as follows (Athanasoula et al. 2016):

$$r(x, y) = \left( |x - x_c|^{C_0+2} + \left| \frac{y - y_c}{q} \right|^{C_0+2} \right)^{\frac{1}{C_0+2}}. \quad (7)$$



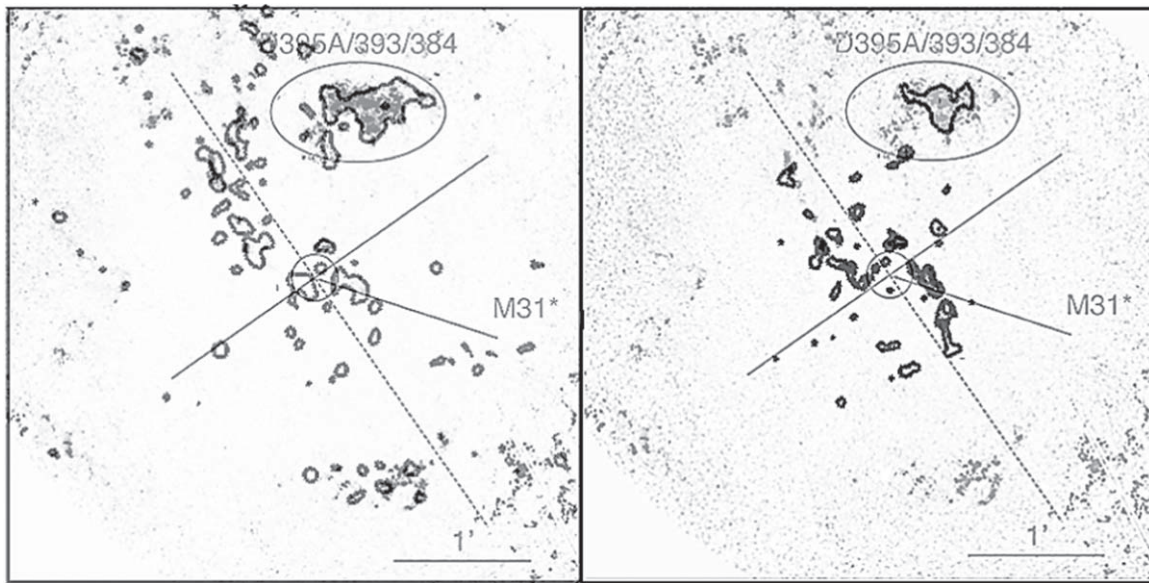


**Figure 7.** Overlays of nuclear spiral dust lane features from UVIT on the grayscale extinction map of Dong et al. (2016): N279N residual image negative contours (left panel) and F148W residual image negative contours (right panel).

$C_o$  is the parameter that controls the diskiness or boxiness of the isophotes (lines of constant  $r(x, y)$ ). For  $C_o = 0$  the isophotes are perfect ellipses. For  $C_o < 0$  the isophotes become more disk-like or disky as  $C_o$  becomes more negative. For  $C_o > 0$  the isophotes become more boxy as  $C_o$  becomes more positive. Table 9 shows results of fitting generalized ellipses for the five UVIT images. All values of  $C_o$  are  $> 0$ , showing that the M31 bulge has a boxy shape.

The second method is to fit radial functions modified by azimuthal functions in GALFIT, as described in Peng et al. (2010). The  $m = 4$  Fourier mode describes whether the bulge is boxy or disky. Table 9 shows the results of fitting the bulge including the  $m = 4$  Fourier mode. For all five UVIT images the boxiness of the bulge is significant (amplitude  $> 0$  at  $7\sigma - 25\sigma$ ). The Fourier mode and  $C_o$  tests of boxiness are consistent for each image: boxiness is strongest for the F148W image, less strong for the F172M image, even less strong for the F169M and N279N images, and weakest but still significant for the N219M image.

#### 4.5. The Nuclear Spiral and Dust Absorption Features

The nuclear spiral is a noticeable feature of the central  $4'$  of the bulge of M31 at specific wavelengths. It is observable in optical emission lines S II, O III (Jacoby et al. 1985), and  $H\alpha$  (Li et al. 2009); in radio (Walterbos & Graeve 1985); in infrared emission (Li et al. 2009); and as extinction features found by analysis of broadband optical filters (Dong et al. 2016). The nuclear spiral increases in radius in a clockwise direction. It is not clear from optical images which direction the outer main spiral arms increase in radius (e.g., using the Digitized Sky Survey images of M31). Doppler shifts (Rubin & Ford 1970) clearly indicate that the NE of M31 is moving away from the observer and the SW is moving toward the observer. Tenjes et al. (2017) use deprojected Herschel  $250 \mu\text{m}$  and GALEX NUV images to visualize the spiral arm structure of M31. Their work indicates that the arms increase in radius in a clockwise direction, similar to the nuclear spiral, but with a smaller increase in radius with angle.

In ultraviolet, the bulge is dominated by smooth emission (e.g., Figure 1). In order to see the fine structure of the central region of the bulge in ultraviolet, one has to subtract the large-scale distribution of the light. We subtracted our best-fit bulge model to obtain the residual image of the central part of M31. The sequence of images in Figure 3 shows that as the bulge model improves, the dust lanes in the center of the bulge become more visible.

The nuclear spiral is  $\sim 4'$  in diameter; thus, we show in Figure 6 the contour lines of residual images (size  $250'' \times 250''$ ) around the center of M31 for the five UVIT filters. The contour lines are at negative values in the residual images to emphasize the dust absorption features. The sixth panel of Figure 6 is the extinction map from Dong et al. (2016) for comparison. Figure 7 shows the overlay of the inner  $250'' \times 250''$  of the UVIT residual image contour lines and the extinction map of Dong et al. (2016). The nuclear spiral is clearly visible. Radial velocity studies show that the nuclear spiral is offset radially from the M31 nucleus by less than 50 pc, placing the spiral near the center of the bulge (Dong et al. 2016). The large clump (marked with an ellipse) north of the center is a dust cloud in front of the bulge along our line of sight (Melchior et al. 2000). The close match between the dust lanes detected in the UVIT images and the extinction map of Dong et al. (2016) serves as a verification of our modeling procedure and the best-fit bulge models obtained.

## 5. Conclusion

The nuclear region of M31 is dynamically and photometrically distinct from the bulge and the large-scale galactic disk (Kormendy & McClure 1993; Lauer et al. 1993). Here we construct models of the luminosity distribution of the bulge at NUV and FUV wavelengths using UVIT observations with  $1''$  spatial resolution. The initial fits omit the nuclear region, and then we include the nuclear region. The best-fit multi-component model for the F148W image, which has the highest sensitivity of the five UVIT images, has eight components, with three components for the bulge and five for the nuclear

region (Table 7). These components have different centers, sizes, and ellipticities and are required to fit the asymmetric shape of M31's bulge. The eight-component model very well describes the smooth part of the light distribution so that the residual image can be used to study the sharper features such as dust absorption lanes.

One-component models of the light distribution for M31's bulge region are useful to compare to previous studies at other wavelengths. The Sérsic indices for the five UVIT FUV and NUV bands are  $\simeq 2.5$  for 148, 169, 172, and 219 nm and  $\simeq 2.1$  for 279 nm. The 279 nm value is consistent with Sérsic indices found for M31 previously. The  $R_e$  values are  $\simeq 0.46$ – $0.67$  kpc, which are slightly smaller than values found from *I*-band and  $3.6 \mu\text{m}$  images. The observed images and the model images show strong boxiness, which is confirmed by fitting using boxiness parameters in GALFIT. The Sérsic indices are intermediate between typical values for a classical bulge  $> 2.5$  and typical values for a pseudobulge ( $\sim 1$ – $2$ ), which indicates that M31's bulge likely has both classical and pseudobulge components. The boxiness also argues for a significant pseudobulge component.

Residual images for the five UVIT images were generated by subtracting the best-fit model for each filter from the observed brightness distribution. The residual images were used to map the dust lanes associated with the nuclear spiral that would otherwise be hidden by the bright starlight in the bulge region. The FUV and NUV dust lanes match closely the dust lanes seen in optical extinction (Dong et al. 2016).

There is substantial agreement between our results and the conclusions of other studies on the nature of the bulge of M31 (Blaña Díaz et al. 2018; Saglia et al. 2018) and on the location of the nuclear spiral dust lanes (Li et al. 2009; Dong et al. 2016). This serves as a verification of our model fitting procedure and model results. In future studies, we plan to take advantage of the  $1''$  resolution of the UVIT images to study the complex structure of the other components of M31, such as the disk, spiral arms, and halo.

This work was supported by a grant from the Canadian Space Agency. The authors thank the reviewer for making a number of suggestions to improve this manuscript.

## Appendix

### Models for the M31 Bulge for UVIT F169M, F172M, N219N, and N279N Data

Similar to the F148W image fitting, the four UVIT images (F169M, F172M, N219M, and N279N) were fit with two-dimensional brightness profiles with the inclusion of the dust mask (exclusion of the dust lanes) and with fits for the brightest

stars in the image (similar to Table 2 for the F148W image). One-component fits were carried out including the nucleus mask (i.e., excluding the nuclear region) with a Sérsic function in order to be able to compare to the one-component Sérsic function fit for the F148W image.

Table 8 lists the parameters for the one-component Sérsic model fits for all five images, including F148W. The typical Sérsic index for the one-Sérsic fits (Table 8) is  $\simeq 2.5$  for the four shortest-wavelength filters but close to 2.1 for the longest-wavelength N279N filter. All filters yield the same position angle and nearly the same axis ratio for the bulge. A possible reason that the N279N fit is somewhat of an outlier in Sérsic index is that it is sensitive to different stars in a significant way compared to the shorter-wavelength NUV and FUV filters. For example, as noted in Section 4.2, the short-wavelength filters are sensitive to hot stars (such as extreme horizontal branch stars), whereas N279N is more sensitive to intermediate-temperature stars.

Like the F148W image, the other four UVIT images are significantly better fit by including additional model components. For this set of fits the nuclear region is included (we omit the nuclear mask). Rather than carrying out the full procedure outlined in Figure 2, we only tested Sérsic functions rather than all five functions listed in Section 2.2.1. This was done for the following reasons: the process of fitting for the F148W image took several months because of the large number of models tested; the goal is to have similar functions for all five images in order to fairly compare the parameters; and the F169M, F172M, N219M, and N279N images are of lower S/N. The simplest multiple-Sérsic model that gave a good fit for the F169M, F172M, N219M, and N279N images was a three-Sérsic function model for the bulge plus a single-Sérsic function for the nuclear region, called the 3+1 Sérsic model here. Because the F169M, F172M, N219M, and N279N images had lower S/N than the F148W image (by a factor of  $\sim 2$ – $3$ ; see Table 1), models more complex than four Sérsic components were not justified, that is, the statistical improvement in the fits was not significant. The results of the 3+1 Sérsic model fits are shown in Table 10.

Comparison of the fits between different filters for the 3+1 Sérsic models shows a significant variation in Sérsic indices. As discussed in Section 4.3, the interpretation of the multiple-component fits is not clear: it is basically a phenomenological model for the asymmetric light distribution. The 3+1 Sérsic models have components with a range of indices (excluding the nucleus Sérsic index) from  $\sim 0.4$  to 3.5, with all indices but one (the index for the third component of the F172M image) less than 2.

**Table 10**  
3+1 Sérsic Parameters for the F169M, F172M, N219M, and N279N Images<sup>a</sup>

Image	Component	Magnitude	$R_e$ (arcseconds or kpc) <sup>b</sup>	Sérsic Index	Axis Ratio	Position Angle (deg)
F169M	Bulge					
	Sérsic	$13.4 \pm 0.3$	$480 \pm 120$ ( $1.83 \pm 0.46$ )	$0.87 \pm 0.08$	$0.410 \pm 0.003$	$-30.6 \pm 0.6$
	Sérsic	$13.47 \pm 0.06$	$119 \pm 5$ ( $0.452 \pm 0.019$ )	$1.84 \pm 0.03$	$0.780 \pm 0.002$	$-57.4 \pm 0.4$
	Sérsic	$14.94 \pm 0.45$	$420 \pm 170$ ( $1.60 \pm 0.65$ )	$0.36 \pm 0.02$	$0.200 \pm 0.003$	$75.9 \pm 0.7$
Nucleus	Sérsic	$18.34 \pm 0.02$	$3.1 \pm 0.1$ ( $0.0120 \pm .0004$ )	$2.44 \pm 0.12$	$0.87 \pm 0.03$	$-49.3 \pm 8.6$
F172M	Bulge					
	Sérsic	$14 \pm 7$	$2530 \pm 170$ ( $9.63 \pm 0.66$ )	$0.42 \pm 0.03$	$0.04 \pm 0.24$	$-39.8 \pm 0.6$
	Sérsic	$14.2 \pm 0.4$	$265 \pm 33$ ( $1.00 \pm 0.13$ )	$1.70 \pm 0.12$	$1.00 \pm 0.01$	n/a
	Sérsic	$14.2 \pm 0.6$	$250 \pm 120$ ( $0.95 \pm 0.46$ )	$3.46 \pm 0.36$	$0.750 \pm 0.003$	$-54.4 \pm 0.7$
	Nucleus					
Sérsic	$20.61 \pm 0.03$	$0.99 \pm 0.07$ ( $0.0038 \pm 0.0003$ )	$1.16 \pm 0.28$	$0.88 \pm 0.07$	$67 \pm 24$	
N219M	Bulge					
	Sérsic	$10.34 \pm 2.9$	$1138 \pm 12$ ( $4.331 \pm 0.046$ )	$0.81 \pm 0.14$	$0.73 \pm 0.02$	$-20 \pm 5$
	Sérsic	$12.50 \pm 1.0$	$660 \pm 370$ ( $2.5 \pm 1.4$ )	$1.02 \pm 0.17$	$0.46 \pm 0.01$	$-46.3 \pm 0.6$
	Sérsic	$13.91 \pm 0.05$	$95 \pm 3$ ( $0.362 \pm 0.011$ )	$1.42 \pm 0.02$	$0.860 \pm 0.003$	$-56 \pm 1$
	Nucleus					
Sérsic	$18.36 \pm 0.07$	$5.3 \pm 0.7$ ( $0.020 \pm 0.003$ )	$3.57 \pm 0.34$	$0.78 \pm 0.04$	$-49 \pm 6$	
N279N	Bulge					
	Sérsic	$11.86 \pm 0.18$	$242 \pm 2$ ( $0.921 \pm 0.008$ )	$1.82 \pm 0.01$	$0.730 \pm 0.004$	$-31.7 \pm 0.6$
	Sérsic	$11.97 \pm 0.63$	$500 \pm 160$ ( $1.90 \pm 0.61$ )	$0.93 \pm 0.10$	$0.70 \pm 0.078$	$-55.0 \pm 0.8$
	Sérsic	$12.72 \pm 0.26$	$295 \pm 41$ ( $1.12 \pm 0.16$ )	$1.62 \pm 0.07$	$0.530 \pm 0.005$	$-73.8 \pm 0.7$
	Nucleus					
Sérsic	$16.58 \pm 0.54$	$40 \pm 34$ ( $0.15 \pm 0.13$ )	$6.8 \pm 1.6$	$0.67 \pm 0.04$	$49 \pm 5$	

**Notes.**

<sup>a</sup> The parameters for the 3+1 Sérsic model for the F148W image are given by the four-component model in Table 7.

<sup>b</sup>  $R_e$  in kiloparsecs is given in parentheses.

**ORCID iDs**

Denis Leahy  <https://orcid.org/0000-0002-4814-958X>  
Joseph Postma  <https://orcid.org/0000-0002-3025-1412>

**References**

- Athanassoula, E., Rodionov, S. A., Peschken, N., et al. 2016, *ApJ*, **821**, 90  
 Barmby, P., Ashby, M. L. N., Bianchi, L., et al. 2006, *ApJL*, **650**, L45  
 Beaton, R. L., Majewski, S. R., Guhathakurta, P., et al. 2007, *ApJL*, **658**, L91  
 Bekki, K. 2010, *MNRAS*, **401**, L58  
 Berman, S. 2001, *A&A*, **371**, 476  
 Berman, S., & Loinard, L. 2002, *MNRAS*, **336**, 477  
 Blańa Dfraz, M., Gerhard, O., Wegg, C., et al. 2018, *MNRAS*, **481**, 3210  
 Bournaud, F., Jog, C. J., & Combes, F. 2005, *A&A*, **437**, 69  
 Brooks, A., & Christensen, C. 2016, *Galactic Bulges* (Cham: Springer), 317  
 Caon, N., Capaccioli, M., & D'Onofrio, M. 1993, *MNRAS*, **265**, 1013  
 Chemin, L., Carignan, C., & Foster, T. 2009, *ApJ*, **705**, 1395  
 Choi, P. I., Guhathakurta, P., & Johnston, K. V. 2002, *AJ*, **124**, 310  
 Courteau, S., de Jong, R. S., & Broeils, A. H. 1996, *ApJL*, **457**, L73  
 Courteau, S., Widrow, L. M., McDonald, M., et al. 2011, *ApJ*, **739**, 20  
 de Souza, R. E., & Dos Anjos, S. 1987, *A&AS*, **70**, 465  
 de Vaucouleurs, G. 1974, in *IAU Symp. 58, The Formation and Dynamics of Galaxies*, ed. J. R. Shakeshaft (Dordrecht: Reidel), 335  
 Dong, H., Li, Z., Wang, Q. D., et al. 2016, *MNRAS*, **459**, 2262  
 Dong, H., Olsen, K., Lauer, T., et al. 2018, *MNRAS*, **478**, 5379  
 Dorman, C. E., Widrow, L. M., Guhathakurta, P., et al. 2013, *ApJ*, **779**, 103  
 D'Souza, R., & Bell, E. F. 2018, *NatAs*, **2**, 737  
 Erwin, P., Saglia, R. P., Fabricius, M., et al. 2015, *MNRAS*, **446**, 4039  
 Feng, Z.-X., Li, Z., Shen, J., et al. 2022, *ApJ*, **933**, 233  
 Fisher, D. B., & Drory, N. 2008, *AJ*, **136**, 773  
 Fisher, D. B., & Drory, N. 2010, *ApJ*, **716**, 942  
 Fisher, D. B., & Drory, N. 2016, *Galactic Bulges* (Cham: Springer), 41  
 Gadotti, D. A. 2008, *MNRAS*, **384**, 420  
 Geehan, J. J., Fardal, M. A., Babul, A., et al. 2006, *MNRAS*, **366**, 996  
 Gordon, K. D., Bailin, J., Engelbracht, C. W., et al. 2006, *ApJL*, **638**, L87  
 Guedes, J., Callegari, S., Madau, P., et al. 2011, *ApJ*, **742**, 76  
 Hammer, F., Yang, Y. B., Wang, J. L., et al. 2018, *MNRAS*, **475**, 2754  
 Häußler, B., Bamford, S. P., Vika, M., et al. 2013, *MNRAS*, **430**, 330  
 Häußler, B., Barden, M., & McIntosh, D. H. 2008, in *AIP Conf. Proc. 1082, Classification and Discovery in Large Astronomical Surveys* (Melville, NY: AIP), 137  
 Häußler, B., McIntosh, D. H., Barden, M., et al. 2007, *ApJS*, **172**, 615  
 Ibatá, R., Irwin, M., Lewis, G., et al. 2001, *Natur*, **412**, 49  
 Immeli, A., Samland, M., Gerhard, O., et al. 2004, *A&A*, **413**, 547  
 Jacoby, G. H., Ford, H., & Ciardullo, R. 1985, *ApJ*, **290**, 136  
 Kent, S. M. 1983, *ApJ*, **266**, 562  
 Kent, S. M. 1989, *AJ*, **97**, 1614  
 Keselman, J. A., & Nusser, A. 2012, *MNRAS*, **424**, 1232  
 Kormendy, J., & Barentine, J. C. 2010, *ApJL*, **715**, L176  
 Kormendy, J., & Bender, R. 1999, *ApJ*, **522**, 772  
 Kormendy, J., & Kennicutt, R. C. 2004, *ARA&A*, **42**, 603  
 Kormendy, J., & McClure, R. D. 1993, *AJ*, **105**, 1793  
 Lauer, T. R., Faber, S. M., Groth, E. J., et al. 1993, *AJ*, **106**, 1436  
 Laurikainen, E., & Salo, H. 2016, *Galactic Bulges* (Cham: Springer), 77  
 Leahy, D., Buick, M., & Leahy, C. 2022a, *AJ*, **164**, 183  
 Leahy, D., Buick, M., Postma, J., et al. 2021a, *AJ*, **161**, 215  
 Leahy, D., Morgan, C., Postma, J., et al. 2021b, *IJAA*, **11**, 151  
 Leahy, D., Seminoff, N., & Leahy, C. 2022b, *AJ*, **163**, 138  
 Leahy, D. A., Bianchi, L., & Postma, J. E. 2018, *AJ*, **156**, 269  
 Leahy, D. A., Postma, J., Chen, Y., et al. 2020, *ApJS*, **247**, 47  
 Li, Z., Wang, Q. D., & Wakker, B. P. 2009, *MNRAS*, **397**, 148  
 Lindblad, B. 1956, *StoAn*, **19**, 2  
 Lütticke, R., Dettmar, R.-J., & Pohlen, M. 2000, *A&AS*, **145**, 405  
 McConnachie, A. W., Ibatá, R., Martin, N., et al. 2018, *ApJ*, **868**, 55  
 McConnachie, A. W., Irwin, M. J., Ferguson, A. M. N., et al. 2005, *MNRAS*, **356**, 979  
 Meert, A., Vikram, V., & Bernardi, M. 2013, *MNRAS*, **433**, 1344  
 Melchior, A.-L., Viallefond, F., Guélin, M., et al. 2000, *MNRAS*, **312**, L29  
 Mould, J. 2013, *PASA*, **30**, e027

- Naab, T., & Burkert, A. 2003, *ApJ*, 597, 893
- Noguchi, M. 1999, *ApJ*, 514, 77
- Opitsch, M., Fabricius, M. H., Saglia, R. P., et al. 2018, *A&A*, 611, A38
- Peng, C. Y. 2002, *AJ*, 124, 294
- Peng, C. Y., Ho, L. C., Impey, C. D., et al. 2002, *AJ*, 124, 266
- Peng, C. Y., Ho, L. C., Impey, C. D., et al. 2010, *AJ*, 139, 2097
- Postma, J. E., & Leahy, D. 2017, *PASP*, 129, 115002
- Press, W. H., Teukolsky, S. A., Vetterling, W. T., et al. 1992, Numerical Recipes in FORTRAN. The Art of Scientific Computing (2nd ed.; Cambridge: Cambridge Univ. Press)
- Price, S. H., Kriek, M., Feldmann, R., et al. 2017, *ApJL*, 844, L6
- Querejeta, M., Schinnerer, E., Meidt, S., et al. 2021, *A&A*, 656, A133
- Rosenfield, P., Johnson, L. C., Girardi, L., et al. 2012, *ApJ*, 755, 131
- Rubin, V. C., & Ford, W. K. 1970, *ApJ*, 159, 379
- Saglia, R. P., Fabricius, M., Bender, R., et al. 2010, *A&A*, 509, A61
- Saglia, R. P., Opitsch, M., Fabricius, M. H., et al. 2018, *A&A*, 618, A156
- Sandage, A. 1961, *ApJ*, 133, 355
- Scannapieco, C., White, S. D. M., Springel, V., et al. 2011, *MNRAS*, 417, 154
- Seigar, M. S., Barth, A. J., & Bullock, J. S. 2008, *MNRAS*, 389, 1911
- Simmons, B. D., & Urry, C. M. 2008, *ApJ*, 683, 644
- Singh, K. P., Tandon, S. N., Agrawal, P. C., et al. 2014, *Proc. SPIE*, 9144, 91441S
- Stark, A. A. 1977, *ApJ*, 213, 368
- Stark, A. A., & Binney, J. 1994, *ApJL*, 426, L31
- Tanaka, M., Chiba, M., Komiyama, Y., et al. 2010, *ApJ*, 708, 1168
- Tandon, S. N., Subramaniam, A., Girish, V., et al. 2017, *AJ*, 154, 128
- Tenjes, P., Tuvikene, T., Tamm, A., et al. 2017, *A&A*, 600, A34
- Tonini, C., Mutch, S. J., Croton, D. J., et al. 2016, *MNRAS*, 459, 4109
- Toomre, A. 1977, Evolution of Galaxies and Stellar Populations (New Haven, CT: Yale Univ. Observatory), 401
- Tuccillo, D., Huertas-Company, M., Decencière, E., et al. 2018, *MNRAS*, 475, 894
- Veljanoski, J., Mackey, A. D., Ferguson, A. M. N., et al. 2014, *MNRAS*, 442, 2929
- Walterbos, R. A. M., & Graeve, R. 1985, *A&A*, 150, L1
- Widrow, L. M., Perrett, K. M., & Suyu, S. H. 2003, *ApJ*, 588, 311
- Wuyts, S., Förster Schreiber, N. M., van der Wel, A., et al. 2011, *ApJ*, 742, 96